The role of aerosols and meteorological conditions in shaping cloud droplet development in New Mexico summer deep-convective systems

Huihui Wu[1*], Nicholas Marsden[2], Paul Connolly[1], Michael Flynn[1], Paul I. Williams[2], Declan Finney[3], Kezhen Hu[1], Graeme J. Nott[4], Navaneeth Thamban[1], Keith Bower[1], Alan Blyth[3], Martin Gallagher[1] and Hugh Coe[1,2]

[1]Department of Earth and Environmental Sciences, University of Manchester, Manchester, UK
[2]National Centre for Atmospheric Science, University of Manchester, Manchester, UK
[3]School of Earth & Environment, University of Leeds, Leeds, UK
[4]FAAM Airborne Laboratory, Cranfield, UK
*Now at: Univ Paris Est Créteil and Université Paris Cité, CNRS, LISA, 94010 Créteil, France

Correspondence to: Hugh Coe (hugh.coe@manchester.ac.uk)

Abstract. The accurate representation of aerosol physicochemical properties is important when describing aerosol-cloud interactions. The Deep Convective Microphysics Experiment (DCMEX) aimed to improve the representation of microphysical processes in deep convective systems. As part of this project, an airborne campaign (July to August 2022) was conducted to characterize the thermodynamics-dynamic-aerosol-cloud system over the isolated Magdalena Mountains in New Mexico, US. Backward dispersion analyses identified a transition in dominant airmass origins from Northwest (NW) continental to Southeast (SE) aged oceanic flow, coinciding with substantial changes in meteorological conditions and aerosol characteristics. The SE-flow period generally exhibited lower lifting condensation levels, enhanced convection, higher boundary layer humidity, and more frequent and intense precipitation, compared to the NW-flow period. During the SE-flow period, aerosol size distributions showed a more pronounced bimodality, characterized by increased Aitken-mode concentrations and fewer but larger accumulation-mode particles, indicating enhanced cloud processing. Submicron aerosols exhibited larger sulfate fractions, more oxidized organics, and greater hygroscopicity. Correspondingly, clouds presented larger droplet sizes and liquid water contents. A bin-microphysics parcel model was also employed to simulate the development of cloud droplets, constrained by airborne observations. Model-observation comparisons highlight the critical role of aerosol entrainment in reproducing the observed broad cloud droplet spectra extending toward small sizes. The results underscore the combined influence of meteorological conditions and aerosol characteristics on cloud microphysics under different flow regimes and emphasize the importance of aerosol entrainment in the development of deep convective clouds. This study provides valuable constraints for improving parameterizations of aerosol-cloud interactions in convective systems.

1 Introduction

Deep convective clouds play a crucial role in driving precipitation patterns, the hydrological cycle, and large-scale circulation (Houze, 2014). These clouds also influence the regional and global radiation budget by reflecting incoming solar

radiation and absorbing terrestrial longwave radiation (Jensen and Del Genio, 2003). Furthermore, deep convective cloud systems are likely associated with extreme weather events such as severe thunderstorms, tornadoes, and flash floods, which result in global economic losses (Newman and Noy, 2023). Given their significant effects on the climate system, the accurate

35 representation of deep convective clouds and their microphysical processes in models remains a long-standing challenge for improving weather and climate predictions.

The life cycle of deep convective clouds is modulated by complex microphysical processes, including droplet formation, droplet growth through condensation and coalescence, thermodynamic phase transitions between liquid droplets and ice crystals, and the development of precipitation (Arakawa, 2004). These processes are initiated from droplet formation that

40 mostly occurs at the cloud base. Droplet formation is governed by water vapor supersaturation in updrafts and aerosol physiochemical properties such as concentration, size distribution, chemical composition, and hygroscopicity. Aerosols can also promote the thermodynamic phase transition stage. These aerosol impacts on the formation and development of liquid and ice clouds depend on their roles as cloud condensation nuclei (CCN) and ice nucleating particles (INP). However, aerosol-cloud interaction remains one of the largest uncertainties in predicting climate change and extreme weather (Rosenfeld et al.,

45 2014).

Previous studies have shown that aerosols may invigorate or inhibit the vertical development of convective clouds and precipitation, depending on atmospheric aerosol and meteorological conditions (Koren et al., 2008; Li et al., 2011; Tao et al., 2012; Koren et al., 2014). A widely studied process is the "cold-phase invigoration" of aerosols (Rosenfeld et al., 2008). In aerosol-rich environments, increased aerosol concentrations promote additional activated cloud droplets, resulting in reduced

50 droplet sizes at cloud base. This is likely to delay coalescence processes and hence the development of warm rain, allowing more cloud water to be lifted to above the freezing level. The subsequent release of additional latent heat from the freezing of this increased amount of cloud water may invigorate updraft intensity at upper levels in the cloud. This process could also induce larger amounts of smaller but longer-lasting ice particles within the stratiform and anvil regions of deep convective clouds. Overall, aerosol microphysical effects could contribute to larger cloud cover, longer cloud lifetime, elevated cloud top,

55 enhanced precipitation rates, and stronger storm electrification in more polluted environments. The influence of "cold-phase invigoration" on the development of deep convective clouds has been studied in many marine and continental areas (Fan et al., 2013; Wang et al., 2014). Recently, Fan et al. (2018) introduced the concept of "warm-phase invigoration", showing that the intrusion of ultrafine particles (<50 nm) into warm, moist, and low-aerosol environments such as the wet-season Amazon can intensify convective updrafts within low and middle cloud layers. The intensification is due to the enhanced condensational

60 heating release driven by the additional activation of added ultrafine particles under elevated water vapor supersaturation above the cloud base. This process tends to increase the amounts of both warm rain and supercooled cloud water with vertical development.

However, the invigoration of deep convective clouds due to aerosol microphysical effects may be suppressed under some conditions, e.g. the presence of giant CCN and the competing influence of aerosol radiative effects. The presence of giant CCN

65 such as coarse-mode sea salt aerosols may inhibit the vertical development of deep convective clouds by producing initial

large droplets and accelerating warm rain formation (Yin et al., 2024). Smoke environments with strongly absorbing aerosols tend to inhibit convection intensity by reducing solar radiation reaching the surface and stabilizing the lower troposphere (Ramanathan et al., 2007; Jiang et al., 2018). The net aerosol effects on the cloud development rely on not only the above-mentioned aerosol properties but also other factors such as meteorological conditions and convective regimes. For example,

70   previous studies demonstrated that moist environments with high relative humidity (RH) may play a role in maintaining the aerosol-induced invigoration of deep convective clouds, by regulating entrainment mixing (Koren et al., 2010). Long-term observations in the US Southern Great Plains also suggest that aerosol-induced invigoration is significant in clouds with warm and low bases, while clouds with cool bases showed no change in cloud-top height and precipitation with aerosol concentrations (Li et al., 2011). A recent study also suggested that existing observational and modelling support of aerosol

75   invigoration has methodological limitations (Varble et al., 2023). For example, observational studies of aerosol invigoration face challenges in understanding aerosol correlations with meteorological conditions, and cloud processes such as entrainment. Varble et al. (2023) proposed that the net impact of aerosol invigoration may be negligible, as the buoyancy enhancement due to additional latent heat release under aerosol-rich conditions may be largely offset by greater condensate loadings.

    Overall, existing studies show that aerosol impacts on the development of deep convective clouds are highly complex,

80   which introduces large uncertainties in understanding the climate effects associated with deep convective systems. Advancing understanding in this area requires coordinated observational and modeling efforts across diverse convective regimes with different aerosol and meteorological conditions. To improve the representation of aerosol-cloud interaction and cloud microphysical processes in deep convective systems, the Deep Convective Microphysics Experiment (DCMEX, July to August 2022) was conducted over the Magdalena Mountains, New Mexico (local time = UTC – 6 hours). Isolated convective clouds

85   can frequently form and develop over these mountains during the summer season in North America, providing ideal laboratory-like conditions for investigating deep convective processes. Earlier studies primarily characterized convective clouds and precipitation development in this area (i.e. Blyth and Latham, 1993). The DCMEX campaign provided coordinated and comprehensive observations of aerosols, cloud microphysics, and thermodynamics of the deep convective system over the Magdalena Mountains, benefiting from significant advances in measurement techniques (Finney et al., 2024). In this study,

90   we focus on the influence of meteorological conditions and aerosol properties on the formation and development of cloud droplets during the campaign, combining observations with bin-microphysics parcel model simulations. This study aims to improve the representation of microphysical processes in this region and similar deep convective systems in future model studies.

2 Methods

95   During the DCMEX field campaign, airborne measurements were carried out using the UK FAAM (Facility for Airborne Atmospheric Measurements) Airborne Laboratory (BAe-146 Atmospheric Research Aircraft), with flight operations centred over the Magdalena Mountains (~33.98°N, ~107.18°W), New Mexico, US. In addition to airborne measurements, Doppler

radars, automated cameras, and ground-based aerosol and meteorology measurements were also deployed during the field campaign. More details on the DCMEX project are provided by Finney et al. (2024). This study focuses on airborne

100 measurements, supplemented by observations from meteorological stations installed at Langmuir Laboratory on the summit of the Magdalena Mountain Range (elevation: ~3240 m above sea level (a.s.l)). A total of 19 scientific flights (designated flight labels from C297 to C315) were performed between July 16 and August 8, 2022. Figure 1a shows flight tracks during the campaign. Each flight took off from Albuquerque International Sunport and normally started with a profile ascent to 8–9 km a.s.l, where a dropsonde (Vaisala RD41) was deployed in the vicinity of the Magdalena Mountains. The flights included a

105 series of straight and level runs (SLRs) for aerosol characterization, which was performed around the mountains prior to the initiation of convective cloud cells and followed a designated kite-shaped pattern (solid red kite in Fig. 1a). The aerosol SLRs were conducted at various altitudes, including low-level, close to cloud-base and high-level runs. Cloud passes typically followed the aerosol runs, allowing for the sampling of developing convective clouds over the Magdalena Mountains at altitudes ranging from close to cloud base to approximately the −20°C isotherm. In some cases, cloud passes were also

110 performed slightly away from the mountains. The FAAM Bae-146 was equipped with a suite of instruments to measure atmospheric dynamics and thermodynamics, including wind speed and direction, temperature (T), RH, etc. A brief description of onboard aerosol (number concentrations, size distributions, and submicron chemical compositions) and cloud (number concentrations and size distributions) measurements used in this study are provided in Sect. 2.1. Ground-based meteorological stations provided surface T, RH, pressure, precipitation intensity, etc.

2.1 Instrumentation

Submicron aerosol chemical compositions were measured using a compact time-of-flight aerosol mass spectrometer (C-ToF-AMS, Aerodyne Research Inc, Billerica, MA, USA) and a Single Particle Soot Photometer (SP2, Droplet Measurement Technologies, Boulder, CO, USA). The AMS can provide online chemical characterization across a range of ion mass-to-charge (m/z) ratios from 10 to 500 (Drewnick et al., 2005). The AMS was calibrated using monodisperse ammonium nitrate

120 and ammonium sulfate particles after each flight. The AMS raw data were processed using the standard SQUIRREL (SeQUential Igor data RetRiEvaL, v.1.60N) TOF-AMS software package. A time- and composition-dependent collection efficiency was applied to the data based on the algorithm by Middlebrook et al. (2012). In this study, the mass concentrations of organics, sulfate, nitrate, and ammonium were determined. Organic fragment marker (m/z 44) was used to estimate the oxygen-to-carbon (O:C) ratio of organics following the methods developed by Aiken et al. (2008). The SP2 can measure the

125 refractory black carbon (hereafter referred to as BC) containing particles with an equivalent spherical diameter in the range of 70–850 nm. It can provide BC mass, size, and mixing state. The SP2 incandescence signal, which is proportional to the mass of BC present in the particle, was calibrated using Aquadag BC standards (Aqueous Deflocculated Acheson Graphite, manufactured by Acheson Inc., USA). Details on the AMS and SP2, including instrument principles as well as operation, calibration, and data interpretation for aircraft deployment have been described previously (Drewnick et al., 2005; Liu et al.,

130 2010; Morgan et al., 2010).

Aerosol size distributions were measured via an on-board scanning mobility particle sizer (SMPS) and a wing-mounted passive cavity aerosol spectrometer probe (PCASP). The SMPS connects a low-pressure water-based condensation particle counter (WCPC model 3786-LP) to a TSI 3081 differential mobility analyser (DMA). It provides aerosol size distribution within the mobility diameter range of 20 to 350 nm, across 40 logarithmically spaced bins. The SMPS data were inverted using
135 the scheme developed by Zhou (2001), based on a ~1 min averaging time. Given the low time resolution, SMPS data were only available during SLRs with relatively stable aerosol levels. The PCASP resolved number concentrations at 5-Hz resolution, across 30 diameter bins between 0.1 and 3 µm. The PCASP was calibrated using di-ethyl-hexylsebacate (DEHS) and polystyrene latex spheres (PSL) with known size and refractive index (Rosenberg et al., 2012). Mie scattering theory was used to determine the bin sizes by assuming particles are spherical, with a refractive index of $1.59 - 0.024i$. Aerosol number
140 concentrations in the accumulation mode (N_a, $0.1 - 3$ µm) were obtained by integrating the PCASP size distributions. A model 3786-LP water-filled condensation particle counter (CPC) on board can detect aerosol particles larger than 2.5 nm (Hering et al., 2005) at 10-Hz resolution, and it can provide number concentrations of all submicron aerosol particles including ultrafine particles (N_{sa}, 2.5 nm to 1 µm) at an accuracy of ±12 %.

Cloud droplet number concentrations and size distributions were measured using a Cloud Droplet Probe (CDP), following
145 the operation and calibration procedures in Lance et al. (2010). The CDP measures the forward scattered light over a 1.7 to 14° solid angle when cloud droplets pass through its incident laser beam. Cloud droplet particles are detected at 25-Hz resolution, and in 30 bins over a nominal size range of 2–50 µm. The size calibrations were performed during pre-flight, using 10 different-size glass beads with known diameters with refractive index (Rosenberg et al., 2012). Conversion from the scattering cross-section to droplet size is done using the refractive index of water, $1.33 + 0i$. The cloud droplet number concentration (N_d),
150 cloud droplet effective radius (R_e), and liquid water content (LWC) were calculated from the CDP's cloud droplet spectrum as follows:

$$N_d = \int n(r) \, dr \approx \sum_1^m n(r_i) \tag{1}$$

$$R_e = \frac{\int r^3 \, n(r) \, dr}{\int r^2 \, n(r) \, dr} \approx \frac{\sum_1^m r_i^3 \, n(r_i)}{\sum_1^m r_i^2 \, n(r_i)} \tag{2}$$

$$LWC = \frac{4\pi}{3} \rho_{water} \int r^3 \, n(r) \, dr \approx \frac{4\pi}{3} \rho_{water} \sum_1^m r_i^3 \, n(r_i) \tag{3}$$

155 where $n(r_i)$ is the number of cloud droplets in a particular size bin, r_i is the middle radius value for each of the size bins, and ρ_{water} is the density of liquid water. An LWC value of 0.01 g m^{-3} was used to define the low threshold for the presence of cloud. To eliminate the inclusion of optically thinner clouds, thresholds of $N_d > 5$ cm^{-3} and bulk LWC from CDP > 0.02 g m^{-3} were used to perform statistical cloud sample analysis.

Table S1 shows a summary of data availability for aerosol and cloud measurements in this study. All aerosol (AMS, SP2,
160 SMPS, PCASP, CPC) and cloud (CDP) measurements were corrected to standard temperature and pressure (STP) (273.15 K and 1013.25 hPa).

2.2 Backward dispersion simulations

To investigate the origin and transport pathways of airmasses over the Magdalena Mountains, backward dispersion simulations were performed using the UK Met Office's Numerical Atmospheric Modelling Environment (NAME) (Jones et al., 2007). NAME was selected for this study due to its ability to utilize high-resolution meteorological data, with a grid resolution of approximately 10 km × 10 km. It is capable of predicting dispersion over a wide range of spatial scales, from a few kilometers to global distances. For each simulation, a specified number of hypothetical tracer particles were released from a 0.2° × 0.2° grid box centered over the Magdalena Mountains (34.0° N, 107.2° W). Low-level and high-level simulations were performed for each flight case separately. Low-level simulations released tracer particles during the time when low-level and below-cloud aerosol runs were conducted, while high-level simulations released particles during high-altitude aerosol samples. The trajectories of released tracer particles were traced backward for 6-days, based on three-dimensional gridded (3D) meteorological fields from the UK Met Office's Unified Model (MetUM) (Brown et al., 2012). These meteorological fields were updated every three hours, with a high horizontal resolution of 0.14° longitude by 0.1° latitude and 59 vertical levels extending up to ~ 29 km in altitude. In this study, the integrated horizontal footprints were output for each simulation, representing the cumulative air parcels passing through each grid over the past 6-days. The footprints are expressed in units of mass concentration (g m^{-3}), based on the predetermined quantity of released air parcels.

2.3 Bin-microphysics parcel model

Simulations of cloud development were conducted using a bin microphysics parcel model (https://github.com/UoM-maul1609/bin-microphysics-model, University of Manchester), an adapted version of the model in Fowler et al. (2020). The bin microphysics model simulates aerosol activation into cloud droplets followed by processes such as condensation and/or deposition from water vapour, collision and coalescence of cloud droplets, and both primary and secondary ice formation processes (James et al., 2023). This study focuses on processes related to the formation and growth of cloud droplets. In the model, aerosol particles are represented by multiple lognormal modes, with each mode treated as an internal mixture with the same chemical composition. The lognormal size distributions of aerosols for each mode are as follows:

$$\frac{dN}{dlnD_a} = \frac{N_T}{\sqrt{2\pi}ln\sigma_g}exp\left[-\frac{ln^2\left(\frac{D_a}{D_{a,m}}\right)}{2ln^2\sigma_g}\right] \tag{4}$$

where N is the number concentration of aerosol particles, D_a is the aerosol particle diameter in the mode, N_T is the total number of aerosol particles in the mode, $D_{a,m}$ is the median aerosol particle diameter for the mode, and σ_g is the geometric standard deviation of the logarithmic distribution. The model is initialized by summing multiple lognormal size distributions.

The activation of aerosol particles is determined by the condensation of water vapor onto aerosol particles, following the equilibrium vapor pressure described by the κ–Köhler theory, which relates aerosol size and hygroscopicity through a single parameter κ (Petters and Kreidenweis, 2007). The subsequent growth of cloud droplets by diffusion accounts for mass accommodation, which is adjusted by modified diffusivity and conductivity (Jacobson, 2005; Pruppacher and Klett, 2010).

Initial cloud droplet growth is governed by the diffusional growth equation, and further growth into raindrops is driven by the collision-coalescence process. The collision–coalescence process is modelled based on the stochastic collection equation using
195   Bott's (1998) method, with collisional efficiencies derived from the Long (1974) kernel. The model employs a binned distribution to represent the size spectrum of liquid droplets, and particles that exceed a diameter of 3 µm are defined as droplets. In the simulations, the initial updraft velocity was specified, with adjustments to account for the effects of buoyancy on the updraft momentum.

In convective clouds, entrainment mixing is the process of incorporating surrounding environmental air into a rising
200   plume. In this study, the simulation of the entrainment process, including both homogenous and inhomogeneous mixing, follows the theoretical framework outlined in Pruppacher and Klett (2010). In the model, the entrainment rate is defined by the ratio of the entrainment parameter (C=0.20) to the radius of the parcel. The air entering the parcel is calculated from thermodynamic profiles of potential temperature and water mixing ratio derived from dropsondes. For homogeneous mixing, entrained subsaturated air uniformly mixes with the cloud parcel, leading to a uniform reduction in droplet size.
205   Inhomogeneous mixing follows similar equations but incorporates different treatments of droplet evaporation and number concentration adjustment (Baker, Corbin, and Latham, 1980). For inhomogeneous mixing, entrained subsaturated air remains in localized pockets rather than mixing instantaneously, leading to the evaporation of some droplets while others are unaffected. This process preserves the initial droplet size distribution but reduces the droplet number concentration. The droplet number concentration in each size bin is adjusted to maintain the relative humidity, preventing a uniform reduction in droplet size as
210   in the homogeneous mixing. Additionally, inhomogeneous mixing remains aerosols released from evaporated droplets in the discrete packets of subsaturated air, within the parcel, which may become re-activated later. More details in the simulations with the entrainment process are given in Sect. 3.3.

3 Results and discussion

3.1 Airmass source and meteorological conditions

215   NAME backward-dispersion fields are used to represent the horizontal footprint of original air parcels transported over the past six days before arriving at the sampling area over the Magdalena Mountains. Figure S1 provides some examples of backward-dispersion fields from selected flight simulations, illustrating different and representative transport pathways of source air parcels before reaching the sampling area during the campaign. In this study, the dispersion regions are classified into four different regions, as shown in Fig. 1a. Figure 1b shows the fractional contributions of different source regions to the
220   air parcels arriving at the sampling area throughout the field experiment, differentiating between low-level (bottom panel) and high-level (top panel) simulations. At the beginning of the campaign from July 16 to 23 (flights C297 to C301), NAME simulations suggest that the majority of air parcels originated from the northwest (NW) area of the Magdalena Mountains. Original air parcels from California were initially transported to the northeast (NE) area before shifting westward (Fig. S1a) or directly moved eastward to the Magdalena Mountains (Fig. S1b), both of which were associated with continental flow. A

225   small fraction of original air parcels arrived from the southeast (SE) area of the Magdalena Mountains, likely carrying aged oceanic airmass from the Gulf of Mexico. Additionally, low-level simulations generally indicate a slightly greater influence of SE-flow compared to high-level simulations. On July 24 (flight C302), NAME simulations indicate a distinct mixture of airmass sources originating from both the NW and SE of the Magdalena Mountains (Fig. S1c). From July 25 to August 1 (flights C303 to C309), the airmass source shifted predominantly to the SE region, with air parcels moving across the Gulf of

230   Mexico and Texas regions (Figs. 1b, S1d, and S1e). Although the long-range airmass sources from August 2 to 4 (flights C310 to C312) remained primarily from the Gulf of Mexico, original air parcels were initially transported to the southwest (SW) and NW areas of the Magdalena Mountains (Arizona and California area) before moving south and eastward (Fig. S1f). This pattern was driven by a temporary shift in local winds, transitioning from southerly to northerly flow around August 3, which returned to southerly before the end of the campaign (Finney et al., 2024). The subsequent days from August 6 to 8 (flights

235   C313-C315) followed a similar source pattern to earlier days (July 25 to August 1, flights C303 to C309) which were dominated by the SE oceanic flow, but with more contributions from the NE continental flow (Fig. S1g).

     For deep-convective cloud systems, the lifting condensation level (LCL) height is considered as a reasonable approximation of cloud base height (Finney et al., 2024). The lifting condensation level temperature (T_{LCL}) and LCL height were calculated using the functions in MetPy Python Package (May et al., 2022), based on the observations of surface T,

240   dewpoint temperature, and pressure from the Magdalena Observatory (Finney et al., 2024). The estimates were averaged over the 15:00–16:00 UTC period, to represent the conditions prior to convection. Figure 2a shows the time series of the estimated T_{LCL} and LCL heights during the DCMEX campaign. At the beginning of the campaign, LCL heights remained relatively high and T_{LCL} remained relatively low. From July 23, LCL heights decreased and T_{LCL} increased substantially. Figure 2b shows the estimated convective available potential energy (CAPE), based on the profiles of T and pressure from dropsonde observations

245   in each flight. CAPE was calculated using the function in MetPy Python Package (May et al., 2022). During the early stage of the campaign (July 16 to 24, flights C297-C302), CAPE values were relatively low, ranging from about 20 to 190 J kg^{-1}. From July 25 (C303 to C309), CAPE increased to an approximate range of 280 to 680 J kg^{-1}, before a general decrease from August 2 (flight C310) onwards. CAPE is suggested to be an indicator of atmospheric instability and the potential for thunderstorm development (Stull., 2016). The observed general increase in CAPE from July 25 (flight C303) occurred with the shift in

250   dominant airmass source from NW to SE, suggesting a higher probability of stronger convection during the SE-flow period. Observations also showed that the SE-flow period had more frequent lightning flashes and higher maximum cloud-top heights over the Magdalena Mountains (Finney et al., 2024), which is consistent with the stronger convection indicated by CAPE. Figures 2c and 2d show the time series of surface RH and T observed at Langmuir Laboratory, along with the corresponding RH and T within 200 m below the LCL height to represent close to cloud-base conditions for each flight. Surface observations

255   generally showed lower RH and higher T during the NW-flow period (prior to July 24) compared to the SE-flow period. As LCL height decreased with the shift in dominant airmass source, the SE-flow period generally had higher T and RH near the LCL (close to cloud-base) compared to the NW-flow period. Figure 2e shows the time series of rain intensity (mm/hr) observed

at the Langmuir Laboratory during the campaign. An increase in the frequency and intensity of precipitation was observed from July 23 (C301).

260   In summary, airmass sources and meteorological conditions in the sampling area exhibited variability throughout the campaign. Two distinct periods are identified, as illustrated in Fig. 1b. During Period 1 (July 19 to 23, flights C297–C301), at the beginning of the campaign, the air mass sources were primarily influenced by NW and/or NE continental flow. This period was generally characterized by relatively weak convection, low LCL heights, low surface RH, and high surface T. During Period 2 (July 25 to August 1 and August 6 to 8, flights C303–C309 and C313–C315), the dominant air mass source

265   transitioned to SE oceanic flow. Compared to Period 1, Period 2 was generally associated with enhanced convection, higher LCL heights, higher surface RH, and lower surface T. This pattern reflects the warmer, drier airmass mainly transported by continental flow from the NW and the cooler, moister airmass originating from the Gulf of Mexico with SE flow. Additionally, there were intermediate days (flights C302 and C310–C312) characterized by a mixture of continental and oceanic air mass sources. The observed variability indicates a potential influence of the source airmass change on meteorological conditions in

270   this region.
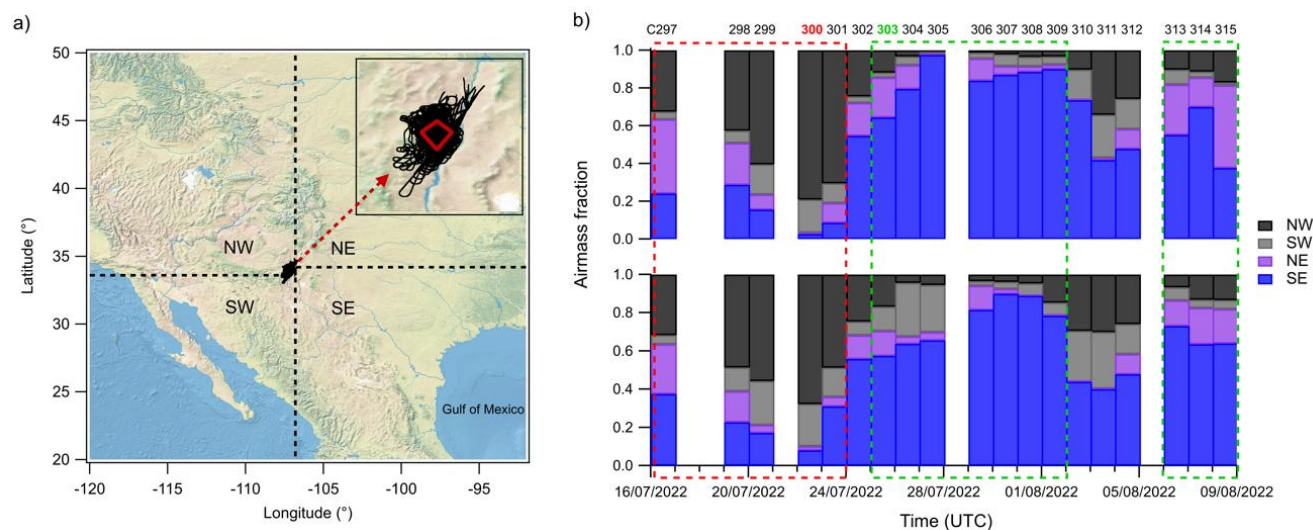
Figure 1. a) Flight tracks during the DCMEX aircraft campaign (designated flight labels from C297 to C315). Each flight followed a designated kite-shaped pattern (red solid lines) over the Magdalena Mountains, New Mexico, USA. Black dashed lines represent four different regions used for air mass source classification. b) Fractional contributions of different source regions to the air parcels
275   **arriving at the sampling area throughout the field experiment. The bottom plot represents low-level simulations, and the upper plot represents high-level simulations. The dashed red box represents flights included in Period 1, and the green boxes represent flights included in Period 2. The corresponding flight numbers are indicated in the plot, and the two flights (C300 and C303) used for case simulations with bin microphysics parcel model are highlighted in red and green colours.**

9
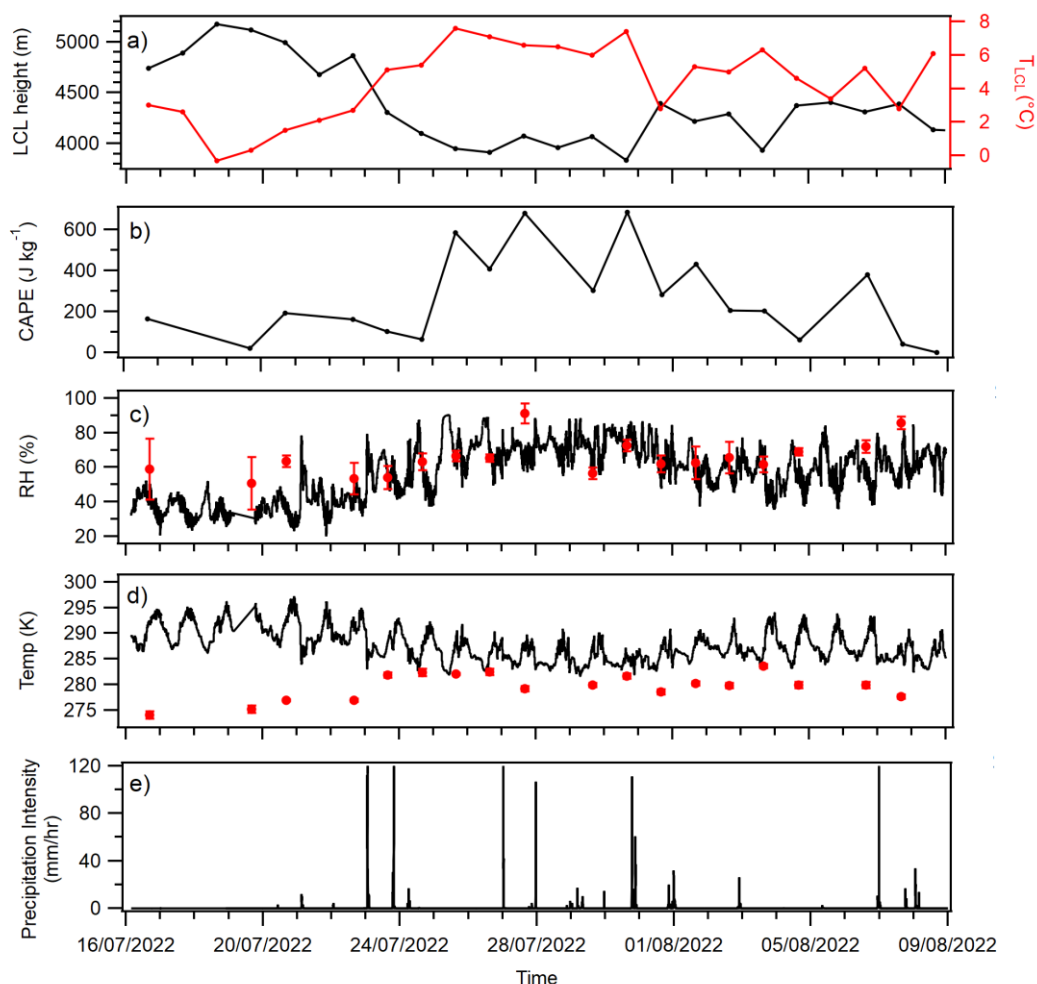
Figure 2. From the top to the bottom: a) Daily LCL (left axis) height and T_{LCL} (right axis) during the DCMEX campaign, which is estimated from Magdalena observations (15:00–16:00 UTC period). b) The calculated convective available potential energy (CAPE), based on dropsonde observations in each flight. c, d) Time series of surface RH and T observed at Langmuir Laboratory, along with the corresponding near cloud-base RH and T for each flight, the red markers and error bars represent averages and standard deviations within 200 m below the LCL height. e) Time series of precipitation intensity observed at Langmuir Laboratory.

3.2 Aerosol Properties

3.2.1 Vertical profile of aerosol concentration

Figures 3a and 3b show the vertical profiles of out-of-cloud aerosol number concentrations from PCASP measurements (N_a, 0.1 to 3 µm) and out-of-cloud submicron aerosol number concentrations from CPC measurements (N_{sa}, 2.5 nm to 1 µm) respectively, for each flight. It should be noted that the y-axis represents the relative altitude with respect to the LCL height, which is an approximation of cloud base height in this study. The corresponding vertical profiles of aerosol number concentrations in terms of absolute altitude (above sea level, a.s.l.) are shown in Fig. S2.

10

At the beginning of the campaign (July 16 to 24, flights C297-C302), aerosols (0.1 to 3 µm) were observed from the surface up to altitudes above the LCL, with relatively constant and high N_a reaching 6–6.5 km a.s.l., followed by a steep decline at higher levels. In the middle of the campaign (July 25 to August 1, flights C303-C309), aerosols (0.1 to 3 µm) were mainly

295 concentrated within the LCL layer. Above the LCL, N_a monotonically decreased with altitude, with minimal amounts observed above 5.5–6 km a.s.l. For the later flights (from August 2, flight C310 onwards), relatively constant N_a generally extended again from the surface up to altitudes slightly above the LCL. Aerosols larger than 0.1 µm are suggested to behave as the dominant CCN in most environments (Dusek et al., 2006; Braga et al., 2022). In this deep-convective cloud system, aerosols larger than 0.1 µm (or CCN) can be activated to produce cloud droplets at/above the cloud base and subsequently removed

300 from the atmosphere through following precipitation, a process known as in-cloud scavenging (rainout). The substantial decrease in N_a above the LCL after July 24 is possibly due to the more efficient in-cloud scavenging on these days, which is indicated by the increase in the frequency and intensity of precipitation from July 23 (Fig. 2e).

The vertical structures of N_{sa} during the campaign followed a temporal evolution pattern similar to that of N_a. However, an enhancement in N_{sa} was observed at high altitudes (> 7 km a.s.l.) in some flights, such as C303-C305. This enhancement

305 of N_{sa} but not N_a suggests the presence of small particles at high altitudes. Similar findings have been reported in other convective regions, including the Pacific and Atlantic oceans and the Amazon Basin (Andreae et al., 2018; Williamson et al., 2019). It is suggested that deep convective clouds are able to transport condensable vapours (such as low-volatility organic compounds and sulfuric acid) into the upper troposphere, where new particle formation (NPF) from detrained condensable vapours may contribute to a large number of ultrafine particles (particles smaller than 50 nm) at high altitudes

310 (Williamson et al., 2019). In addition, deep convective clouds can remove pre-existing large particles that would act as sinks for small particles and condensable vapours, thereby further enabling the occurrence of NPF (Ekman et al., 2006). A recent study in the Amazon Basin highlights the key role of extremely low-volatility organic compounds formed from natural biogenic emissions in driving the NPF process and generating the observed ultrafine particles at Amazon high-altitudes (Zhao et al., 2020). The Magdalena Mountains may serve as a source of biogenic volatile organic compounds (VOCs) emissions

315 from local forests, as documented in previous field studies (e.g. Villanueva-Fierro et al., 2004). During the campaign, the large numbers of ultrafine particles at high altitudes were mainly observed on days with relatively strong convection (from July 25, flight C303 onwards). The observations indicate that NPF may be common at high altitudes in this deep-convective environment, providing an important aerosol reservoir. This aerosol reservoir at high altitudes is significant for the climate system, as the small particles may grow to CCN size locally and impact local anvil and cirrus cloud properties. Possibly more

320 importantly, as the newly formed particles grow with condensation and coagulation processes in subsiding cloud-free air, they may provide an important source of CCN to the lower troposphere and affect low-level cloud properties on regional scales (Williamson et al., 2019).
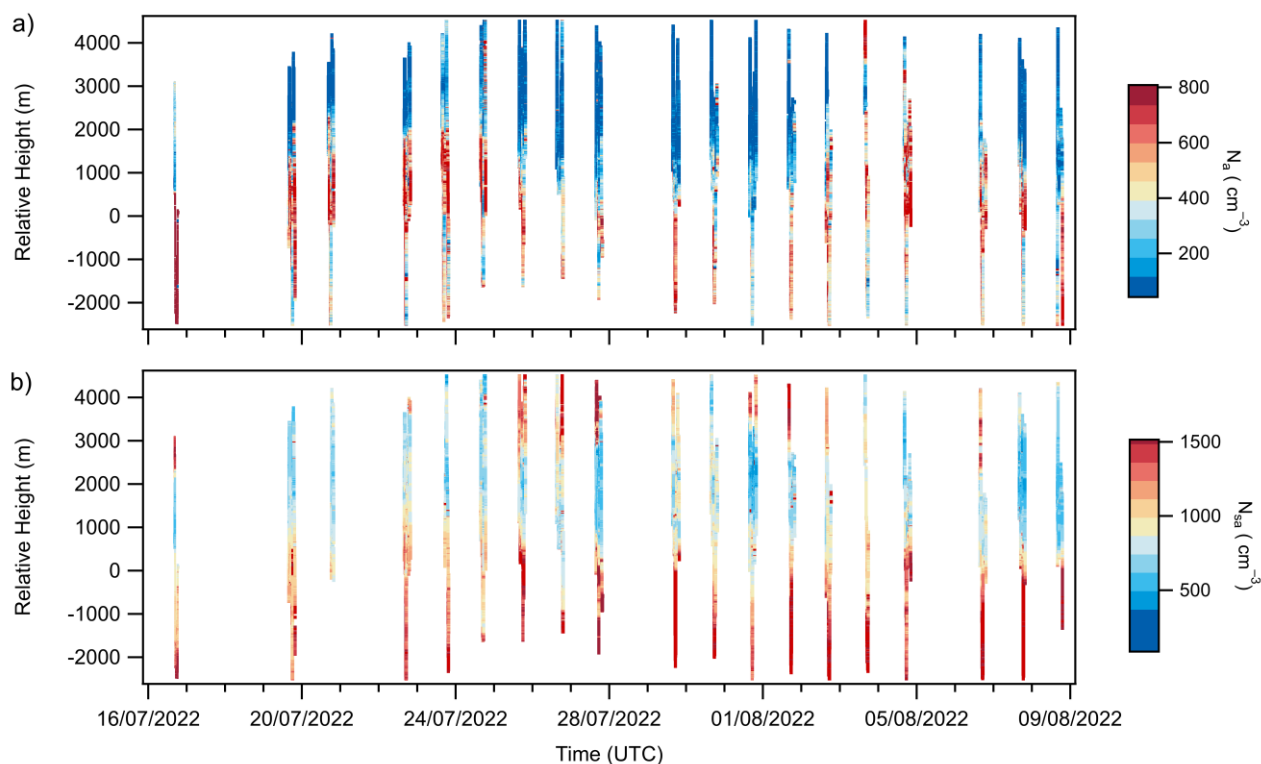
Figure 3. Vertical profiles of a) out-of-cloud N_a (0.1 to 3 µm) number concentrations from PCASP measurements and b) out-of-cloud
N_{sa} (2.5 nm to 1 µm) number concentrations from CPC measurements, for each flight. The y-axis is the relative height with respect
to the LCL height.

3.2.2 Aerosol physicochemical properties

As discussed in previous sections, the airmass sources, meteorological conditions, and vertical aerosol structures in the
sampling area changed during the campaign. Here, available measured and estimated aerosol properties, including aerosol size
distribution, chemical composition and hygroscopic characteristics, are summarized for: 1) Period 1 (available flights include
C298 to C301, conducted from July 19 to 23), representing aerosol properties during the NW-flow (continental flow) period
with relatively weak convection; and 2) Period 2 (available flights include C303 to C309, and C313, conducted from July 25
to August 1 and on August 6), representing aerosol properties during the SE-flow (oceanic flow) period with relatively strong
convection.

Size distribution

Figure 4 shows number size distributions (dN/dlog$_{10}$Dp vs. Dp) and volume size distributions (dV/dlog$_{10}$Dp vs. Dp) of
aerosols measured over near cloud-base SLRs for two periods. The analysis combined measurements from the SMPS and
PCASP, covering a size range from about 20 nm to 3 µm. The corresponding average aerosol number size distributions for
each flight are provided in Fig. S3. During Period 1, aerosol number size distributions for each flight followed a similar pattern

340   in terms of shape and concentration. These distributions were generally characterized by a weakly bimodal structure. The average number size distribution of Period 1 (Fig. 4a) had an Aitken mode with a peak concentration of ~800 cm^{-3} at a diameter near 50 nm and an accumulation mode with a peak concentration of ~2600 cm^{-3} at a diameter near 100 nm. During Period 2, aerosol number size distributions were generally more distinctly bimodal and showed larger variations than those during Period 1 (Fig. S3). Notably, in some flights, e.g. C303, the bimodal size distributions had an Aitken mode and an accumulation mode,

345   with a distinct minimum between the two modes, commonly known as the Hoppel minimum (Hoppel et al., 1985). Compared to Period 1, the average number size distribution of Period 2 (Fig. 4b) presented a more pronounced Aitken mode, with a higher peak number concentration of ~2000 cm^{-3} at a diameter similarly near 50 nm. In contrast, the accumulation mode was relatively reduced, showing a lower peak concentration of ~2000 cm^{-3} at a slightly larger diameter near 115 nm. Though there were differences in number size distributions, the volume size distributions for Periods 1 and 2 were similar, as the aerosols at

350   small sizes (< 0.1 µm) contributed only a small fraction to the total aerosol volume.

The more distinct bimodality observed during Period 2, particularly the Hoppel minimum observed in some flights, suggests that aerosols during Period 2 may have experienced greater cloud processing than those during Period 1. Larger particles are more likely to be activated as cloud droplets, which then either precipitate (in-cloud scavenging) or evaporate to form even larger aerosol particles due to in-cloud chemical processing and coagulation resulting from collisions between cloud

355   droplets. Previous aircraft campaigns over the Amazon Basin reported that the detrained accumulation aerosols from precipitating clouds, which evaporate at the lateral boundaries, have relatively larger sizes but lower concentrations due to cloud-processing and scavenging (Braga et al., 2022). These processes could lead to the accumulation mode with a larger peak diameter and generally lower peak concentration observed during Period 2. The extent of precipitation may also contribute to the variations in the concentration levels of size distributions between individual flights during Period 2. The smaller (Aitken-

360   mode) particles are typically formed from gas-to-particle conversion involving vapors like organic and sulfate vapors. The observed increase in Aitken-mode particle concentrations during Period 2 suggests that changes in source regions and meteorological conditions may have influenced the local gas-to-particle conversion process, as it is sensitive to environmental parameters such as T and RH (Kulmala et al., 2013). The lower surface T during Period 2 likely enhanced gas-particle partitioning by reducing the volatility of semi-volatile compounds, and the more humid boundary layer conditions likely further

365   accelerated growth through the condensation of water-soluble gases.
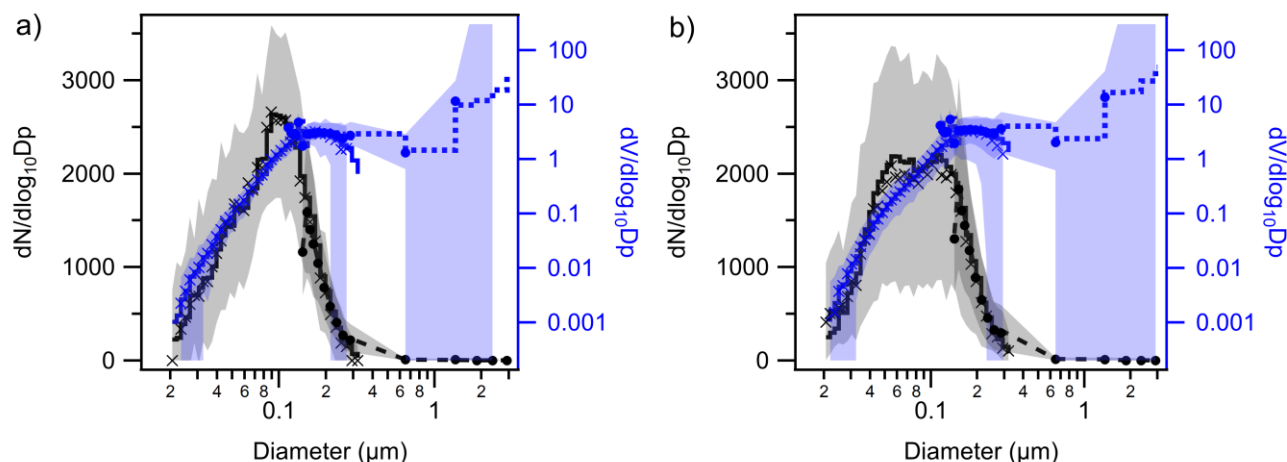
Figure 4. Aerosol size distributions over near cloud-base SLRs for a) Period 1 and b) Period 2. The black lines, markers, and shades show average, median, 10 and 90 percentiles of number size distributions (left axis). The blue lines, markers, and shades show average, median, 10 and 90 percentiles of volume size distributions (right axis). The solid lines and cross markers represent results from SMPS; dashed lines and circle markers represent results from PCASP.

Chemical composition

The average out-of-cloud vertical profiles of mass fractions of different aerosol compositions in the submicron-size range (PM1), measured by the AMS and SP2, are shown in Figs. 5a and 5b for Periods 1 and 2 separately. The corresponding absolute mass concentrations of different aerosol compositions for the two periods are provided in Fig. S4. During Period 1, the dominant PM1 component was organic throughout the aerosol column, followed by inorganic sulfate, ammonium, and nitrate. BC contributed a minor fraction to the total PM1, suggesting a potentially negligible influence of combustion emissions on local aerosol burdens during the campaign. There were variations in chemical composition below and above the LCL, in terms of concentrations and fractional contributions. This variation in aerosol layers may be partly due to slight differences in airmass source contributions at different altitudes, which is supported by NAME backward-dispersion results in Sect. 3.1. Other processes, such as in-cloud scavenging and chemical thermodynamics, may also contribute to this variation. Both absolute and relative sulfate levels were generally lower above the LCL compared to below, as the hygroscopic sulfate aerosols could act as efficient CCN and undergo in-cloud scavenging at and above the cloud base. It is noted that both absolute and relative nitrate levels generally increased with altitude, despite its hygroscopic nature. Inorganic nitrate, in the form of ammonium nitrate (NH_4NO_3), is a semi-volatile species. The colder and moister atmosphere at higher altitudes may promote the condensation of nitrate and ammonia vapors ($HNO_3 + NH_3$) onto existing aerosol particles, which has been reported in previous observational studies (Morgan et al., 2020; Wu et al., 2020). Therefore, the chemical thermodynamics of the HNO_3-NH_3-NH_4NO_3 system across large temperature and RH gradients (Fig. S5) may result in the condensation and formation of NH_4NO_3 above the LCL in this study.

During Period 2, mass concentrations of different aerosol compositions substantially decreased above the LCL, reaching minimal levels at ~1 km above the LCL, which followed the observed N_a pattern. Compared to Period 1, the distinct chemical

14

change during Period 2 was the enhanced inorganic sulfate levels, in terms of absolute mass concentrations below the LCL and its fractional contribution throughout the aerosol column. This change could be due to the large intrusion of marine airmasses from the Gulf of Mexico during Period 2. Marine emissions of dimethyl sulfide (DMS) are the most important biological precursors of global sulfate aerosol, the oxidation of which forms sulfur dioxide (SO_2) and methyl sulfonic acid

395 (MSA) (Hoffmann et al., 2016; Tashmim et al., 2024). SO_2 can be further oxidized by the gas-phase reaction with hydroxyl radical (OH) to form sulfuric acid (H_2SO_4), which is a significant contribution to aerosol nucleation and condensational growth. SO_2 oxidation through aqueous chemistry in cloud droplets, such as the reaction with hydrogen peroxide (H_2O_2), can also contribute to SO_4^{2-} formation. Therefore, marine emissions from the Gulf of Mexico likely contributed to the increase in sulfate levels during Period 2 under SE flow-dominated conditions. Figure 5c shows the vertical profiles of O:C ratios for Periods 1

400 and 2, which is a proxy for the oxidation state of organic matter (Aiken et al., 2008). Another distinct chemical change during Period 2 was the higher O:C ratios compared to Period 1, suggesting a more oxidized organic state or/and a larger fraction of highly oxidized organics. OH radical is the dominant oxidizing agent in the troposphere. Model and satellite studies of global OH distributions have reported more abundant OH at lower latitudes (0–30° N) compared to higher latitudes (Zhao et al., 2019; Pimlott et al., 2022). The organics and organic precursors (VOCs) during Period 2 likely underwent more extensive photo-

405 oxidation while being transported with the SE flow, consequently resulting in the more oxidized organic state.

Hygroscopic parameter

The hygroscopicity of aerosol particles determines their CCN ability to be activated into the cloud droplet, which is related to aerosol chemical compositions and size (Farmer et al., 2015). Kappa (κ), a parameter to evaluate the hygroscopic property of aerosols (Petters and Kreidenweis, 2007), was estimated based on chemical compositions measured by the AMS and SP2

410 (Haslett et al., 2019). In brief, the κ values and volume fractions of different chemical species (such as BC, organics, ammonium sulfate, ammonium nitrate, etc.) were combined to derive a bulk κ for the mixed particles, following the ZSR (Zdanovskii, Stokes and Robinson) mixing rule (Petters and Kreidenweis, 2007). The molar concentrations of different inorganic salts (such as ammonium sulfate, ammonium nitrate, etc.) were established using the measured components (nitrate, sulfate, and ammonium fragments) from the AMS and the ion pairing scheme, as shown in Haslett et al. (2019). Figure 5d

415 shows the vertical profiles of calculated bulk κ values, suggesting generally more hygroscopic PM1 during Period 2 compared to Period 1. The enhanced hygroscopic property of aerosols during Period 2 is likely due to the increase in the fractions of non-sea-salt inorganics in PM1 (Figs. 5a and 5b), as inorganic salts typically have higher κ and are more hygroscopic than organics on a global scale (Pöhlker et al., 2023). Additionally, previous studies indicate that the hygroscopic parameter for organics, κ_{org}, is positively correlated with the organic O:C ratio (Chang et al., 2010; Han et al., 2022). An empirical linear

420 relationship between κ_{org} and O:C ratio ($\kappa_{org} = (0.29 \pm 0.05) * O/C$) was applied in this study, which is based on previous field observations at a rural site subject to biogenic and anthropogenic influence (Chang et al., 2010). The enhanced organic oxidation state during Period 2 may have contributed slightly to the increase in κ_{org} and thus bulk κ. Aerosol observations indicate that the source airmass regions and transport pathways play an important role in modifying aerosol size distributions

and chemical compositions, and subsequently affecting their hygroscopic characteristics in this area, suggesting a potential
425 impact on local cloud formation.
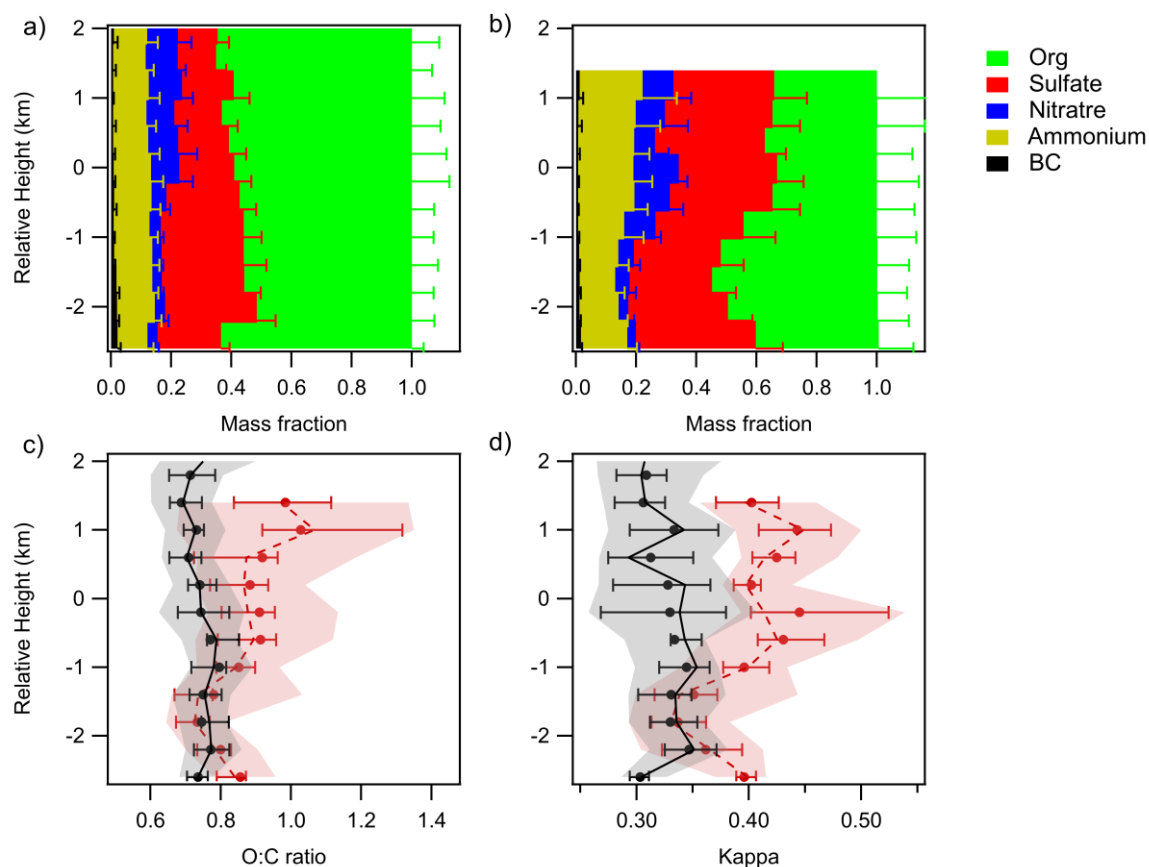
Figure 5. Average vertical profiles of out-of-cloud PM1 chemical composition ratios for a) Period 1 and b) Period 2. The width of colour bars represents the average mass ratios of different species in each vertical bin. The error bars represent standard deviation. c, d) Vertical profiles of c) organic O:C ratio and d) bulk aerosol kappa for Period 1(black) and Period 2 (red). The lines, dots, bars
430 and shades represent median, mean, 10, 25, 75, and 90 percentiles. The y-axis is the relative height with respect to the LCL height.

3.3 Development of liquid clouds in the deep-convective system

3.3.1 Cloud droplet measurements

At the beginning of the campaign (flights C298-C300), the lowest measured cloud layers were at an altitude range of ~
(4.8–5.1) km a.s.l., with ambient T ranging between ~273 and 276 K. From July 23 (flight C301) onward, the lowest measured
435 cloud layers were at a lower altitude range of ~ (3.8–4.4) km a.s.l., with ambient T ranging between ~ 275 and 280 K. Cloud properties in the lowest measured cloud layers during each flight are summarized in Table S2, along with the N_a within 200 m below the LCL height to represent close to cloud-base aerosol (0.1 to 3 µm) concentrations. Approximate distances between the lowest measured cloud layers and the LCL heights are also summarized in Table S2. Altitudes of the lowest measured

440 cloud layers during each flight were generally close to or much higher than the estimated LCL height which approximates cloud base height. It is noted that the actual cloud base could have been below the altitudes of the lowest measured cloud layers. Additionally, vertical profiles of measured cloud droplet properties were analysed to examine the vertical evolution of convective clouds during the campaign. Flights C297, C302, C311, and C315 are excluded from cloud analysis due to the absence of convective clouds or insufficient multi-altitude cloud sampling on those days.

Flights C298 to C301 (belong to Period 1) were characterized as the NW-flow dominated period, associated with relatively
445 weak convection and continentally influenced aerosol characteristics. Average values of below-cloud N_a for these Period 1 flights were similar, in a range of $(533 - 636)$ cm^{-3}, with maximum values reaching $(1198 - 1490)$ cm^{-3}. The lowest measured cloud layers during these flights were consistently close to the estimated LCL heights (near the cloud base). Average values of N_d in these lowest measured cloud layers near the cloud base were in a range of $(521 - 722)$ cm^{-3}, with maximum values reaching $(777 - 1055)$ cm^{-3}. Corresponding average values of LWC and R_e ranged from 0.09 to 0.13 g m^{-3} and 3.2 to 4.1 µm
450 respectively. With similar LCL heights and atmospheric conditions, flights C298 to C300 had relatively consistent vertical development of cloud droplets. Figure 6 (black lines) shows the vertical profiles of N_d, LWC, and R_e observed during flights C298 to C300. There was a slight decrease in N_d in the low cloud layers, followed by relatively constant values with height. The LWC and R_e generally showed increasing trends with height, with some cases decreasing near the tops of the measured cloud layers. Maximum values of LWC and R_e reached $3.2 - 3.7$ g m^{-3} and $10 - 10.4$ µm respectively, at approximately 3.3 to
455 3.8 km above the LCL where T ranged between 248 and 253 K. With a decreased LCL height, Flight C301 showed similar N_d but slightly higher ranges of LWC and R_e compared to earlier Period 1 flights (Fig. S6). Maximum LWC and R_e values reached 5.8 g m^{-3} and 12.2 µm respectively near the top of the measured cloud layers, ~4.8 km above the LCL at the T of ~246 K.

Period 2 (flights C303 to C309, C313 and C314) was characterized as the SE-flow dominated period, associated with additional changes in such as convection and aerosol properties. Compared to Period 1, Period 2 had a broader range of below-
460 cloud N_a, with average values ranging from 298 to 795 cm^{-3} and maximum values between 508 and 1202 cm^{-3}. During Period 2, the LCL heights were decreased compared to Period 1. Due to flight safety restrictions above the Magdalena Mountains, the lowest measured cloud layers were generally well above the cloud base, limiting direct comparisons of the lowest measured cloud layers between Periods 1 and 2. Nevertheless, in a subset of Period 2 flights (C305, C309, C313 and C314), the lowest measured cloud layers were close to the estimated LCL heights (near the cloud base). These cases indicate that near cloud-
465 base LWC (0.16 to 0.35 g m^{-3}) and R_e (3.9 to 5.1 µm) during Period 2 were likely higher than those during Period 1. The vertical profiles of N_d, LWC, and R_e during Period 2 (Fig. 6, red lines) followed similar patterns to Period 1. However, Period 2 flights generally had higher ranges of LWC and R_e at equivalent heights above the LCL, compared to Period 1 flights. For example, in flights C303 to C306, the maximum LWC and R_e values reached $4.7 - 5.8$ g m^{-3} and $11.4 - 13.6$ µm respectively, near the tops of the measured cloud layers at T comparable to those in Period 1 (< 253 K). It is noted that cloud measurements
470 did not extend to the ambient cloud top in this study. Satellite estimates of the maximum cloud top heights are provided in Finney et al (2024), showing generally higher cloud tops during Period 2 ($10.9 - 14.8$ km a.s.l.) compared to Period 1 ($7.6 - 12.7$ km a.s.l.).

17

The decrease in LCL and associated cloud-base heights from July 23 (flight C301), along with higher cloud-base T and P, allowed for a larger amount of water vapour and subsequently led to the observed higher LWC occurred above the cloud base during Period 2 (Pruppacher and Klett, 2010). Compared to Period 1, Period 2 also exhibited significant changes in aerosol amounts and properties. During Period 2, aerosols close to cloud-base were generally more hygroscopic (average κ = 0.34 – 0.53) than those during Period 1 (average κ = 0.27 – 0.38), which was due to changes in aerosol composition associated with airmass source transfer. This suggests that aerosol particles during Period 2 were likely more effective at absorbing water vapour and being activated into cloud droplets at the cloud base (Petters and Kreidenweis, 2007). The critical activation diameter could shift to a lower size during Period 2, driven by the presence of more hygroscopic aerosols. Another distinct change in aerosol properties, as discussed in Sect. 3.2, is the greater variability in aerosol concentrations and size distributions during Period 2. In some flights, the decrease in accumulation-mode particle concentrations may have counteracted the positive effect of enhanced hygroscopicity on aerosol activation and cloud droplet formation at the cloud base. However, increases in Aitken-mode particle concentrations were observed in most of the Period 2 flights, which may have led to more small particles being activated to form additional cloud droplets at and above the cloud base, due to the likely smaller critical sizes for droplet formation during Period 2. A droplet number closure study by Braga et al. (2021) showed that Aitken mode particles, particularly those with high hygroscopicity, can play an important role in cloud-base droplet formation under conditions of low pollution levels and high updraft velocities in convective clouds. Observations and numerical simulations of deep convective clouds over the Amazon also suggest that an increase in Aitken mode particles may also lead to the formation of additional cloud droplets above the cloud base (Fan et al., 2018). In summary, the observed changes in meteorological conditions (higher close to cloud-base T and P) and aerosol properties (varying aerosol concentration and size distributions, greater hygroscopicity) could influence cloud droplet formation and growth in this region, leading to higher ranges of LWC and R_e.

Differences in the formation and vertical evolution of cloud droplets may further influence rain/ice initiation and later precipitation processes in convective cloud systems. Previous studies have suggested that a range of R_e between 12 and 14 µm indicates the height at which raindrops start to form via collision-coalescence (Rosenfeld et al., 2012, Braga et al., 2017a). Additionally, cloud droplet sizes (R_e) play a role in the formation and growth of ice particles. Previous satellite studies reported that glaciation temperatures of convective clouds were strongly dependent on R_e at the −5 °C isotherm, with smaller R_e delaying glaciation (Rosenfeld et al., 2011). At the beginning of the campaign (C298-C300), observed R_e values were mainly below 10 µm, suggesting suppressed conditions for raindrop formation. Moreover, the presence of too small supercooled raindrops at cold temperatures likely inhibited ice production (i.e. riming and shattering) processes, while the precipitation may be overwhelmingly produced by ice processes in deep-convective systems (Korolev et al., 2017). This suppression of both raindrop and ice production was likely linked to the observed absence of precipitation during these days. From July 23 (flight C301) onward, observed R_e values were generally close to or exceeded 12 µm near the tops of measured growing cumulus clouds, suggesting conditions more favourable for raindrop and ice formation, and subsequent precipitation. This aligns with the observed increase in both the frequency and intensity of precipitation starting from July 23 (Fig. 2).
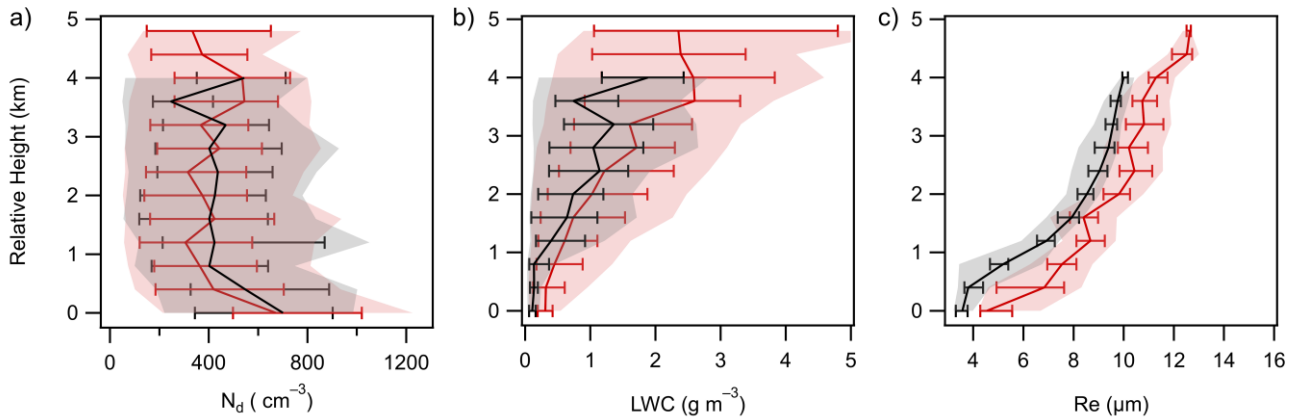
Figure 6. Vertical profiles of a) cloud droplet number concentration (N_d, cm^{-3}), b) liquid water content (LWC, g m^{-3}), and c) effective radius (R_e, µm) for Period 1 earlier flights (black, C298-C300) and Period 2 (red). The lines, bars, and shades represent median, 10, 25, 75, and 90 percentiles. The y-axis is the relative height with respect to the LCL height.

3.3.2 Simulations from bin-microphysical parcel model

Simulations of cloud droplet formation and development were performed using the bin microphysics parcel model for two selected cases (C300 and C303, as highlighted in Fig. 1b), representing Periods 1 and 2 respectively. The initial conditions for model simulations are summarized in Table S3 and Fig. S7, including such as the T, P, RH, aerosol κ and size distributions close to cloud-base derived from airborne measurements. Figure 7 shows the vertical profiles of predicted N_d, LWC, and R_e for the two cases, as well as their comparison with CDP measurements. Additionally, Fig. 8 shows the evolution of the predicted and measured droplet size distributions for the two cases, as a function of T ranging from near cloud base to high level. Simulations assuming adiabatic conditions (Fig. 7, black dashed lines) yielded relatively constant N_d with vertical development, differing from the observed N_d vertical structure, while the predicted LWC and R_e increased with height as did the observations. The adiabatic simulations largely overestimated N_d and LWC. Though the predicted R_e values were only slightly overestimated, the droplet size distributions showed significant differences between the simulations and observations (Fig. 8). Observations of droplet size distributions typically presented bimodal structures, with the width of size distributions increasing with height. In the Period 1 case (C300), CDP observations showed that most droplets near cloud-base had a diameter smaller than 20 µm, which grew to larger sizes with vertical development of clouds. In contrast, the Period 2 case (C303) showed larger and wider size ranges as the cloud developed. However, the adiabatic simulations were much narrower than the observed distributions, which increasingly overestimated the cloud droplet size range as vertical development progressed. Previous adiabatic simulations of deep convective clouds over the Amazon have similarly demonstrated substantial discrepancies between predicted and measured N_d at the cloud base, particularly in cases with high updraft velocities (> 2.5 m s^{-1}) (Braga et al., 2021). Yum and Hudson (2005) also highlighted significant differences in the magnitudes of observed and simulated widths of the size distributions in shallow cumulus clouds from their adiabatic parcel model. These differences in

the predicted and measured convective clouds are attributed to neglecting non-adiabatic processes and/or the entrainment of aerosol particles (Braga et al., 2021).

Many observations and modelling studies have suggested that entrainment and mixing processes are important for the evolution of cloud droplets (Burnet and Brenguier 2007; Lehmann et al., 2009; Braga et al., 2017b). The representation of the

535   entrainment/mixing process in models remains uncertain. It is unclear whether mixing is predominantly homogeneous, inhomogeneous, or a combination of both. For smaller droplets, inhomogeneous mixing typically dominates as the evaporation of cloud droplets is significantly faster than the mixing of cloud with surrounding subsaturated air. When droplets are larger and their evaporation rate becomes more comparable to the mixing rate, homogeneous mixing becomes more dominant, and the influence of inhomogeneous mixing weakens. Some studies suggest that inhomogeneous mixing may dominate in early

540   cloud development when droplets are smaller, and homogeneous mixing may become more prevalent as clouds evolve (i.e. Lehmann et al., 2009). In this study, the entrainment of surrounding air was incorporated into simulations, and the thermodynamic profiles of surrounding air were constrained by dropsonde measurements. The simulations of entrainment began with inhomogeneous mixing at the cloud base during the first 30 seconds of upward transport (reaching ~ 1 km above the cloud base), followed by homogeneous mixing for the rest of the simulation. With the inclusion of entrainment processes,

545   which considered the dilution of cloud layers by entrained subsaturated air and the associated evaporation of cloud droplets, the predicted N_d and LWC were substantially reduced throughout the cloud depth compared to adiabatic simulations. As seen in Fig. 7 (pink dashed lines), the vertical profiles of predicted LWC became relatively consistent with observations. While the predicted N_d values close to cloud base compared relatively well with observations, they showed a more pronounced decline with vertical development, particularly in the Period 1 case. Predicted R_e values were further overestimated, especially at

550   higher cloud levels, which was correlated to the underestimated N_d. Moreover, simulations with entrainment processes continued to produce narrow droplet size distributions, missing small cloud droplets as vertical development progressed (Fig. 8, pink dashed lines).

Previous studies suggest that aerosols entrained with surrounding subsaturated air can be activated in the rising air parcel, broadening droplet size distributions to small droplet diameters (Lehmann et al., 2009; Chandrakar et al., 2016). In this study,

555   aerosol entrainment was further included into the simulations (green dashed lines in Figs. 7 and 8). It is noted that aerosols mixed with the entrainment process were assumed to have same size distributions with that observed close to cloud-base (Fig. S7). The further inclusion of aerosol entrainment made a negligible difference to the predicted LWC. However, the two cases showed different response in simulated N_d and cloud droplet size. In the Period 1 case, predicted N_d, R_e and widths of droplet size distributions showed good agreement with observations. In the Period 2 case, while the inclusion of aerosol entrainment

560   improved simulations, the R_e and droplet size widths were slightly underestimated, associated with overestimated N_d as vertical development progressed. This discrepancy is likely due to different vertical distributions of aerosol concentrations between the two cases, where N_a remained relatively constant above the cloud base in C300 but monotonically decreased in C303. The assumption of constant aerosol size distributions during the entrainment process aligned well with the Period 1 case. However, it likely resulted in overestimated N_d in the Period 2 case, due to excessive entrained aerosols in simulations, which in turn led

565   to underestimated R_e. For cases like C303, the assumption of decreasing aerosol entrainment with altitude should be considered to improve future simulations of the evolution of droplet number and size. Additionally, this discrepancy is likely attributed to the parameterization of the initial radius of ascending cloud parcels in simulations (Table S3). The simulated entrainment rate is sensitive to the parcel radius, with smaller radius resulting in stronger entrainment and more rapid dilution. However, since the initial radius cannot be directly constrained by measurements, this also introduces uncertainty in simulations. In this study,

570   simulations of cloud droplet formation and development based on different assumptions highlight the importance of incorporating the entrainment process of surrounding subsaturated air, particularly aerosol entrainment. The incorporation of aerosol entrainment is crucial in reproducing the width of droplet size distributions.
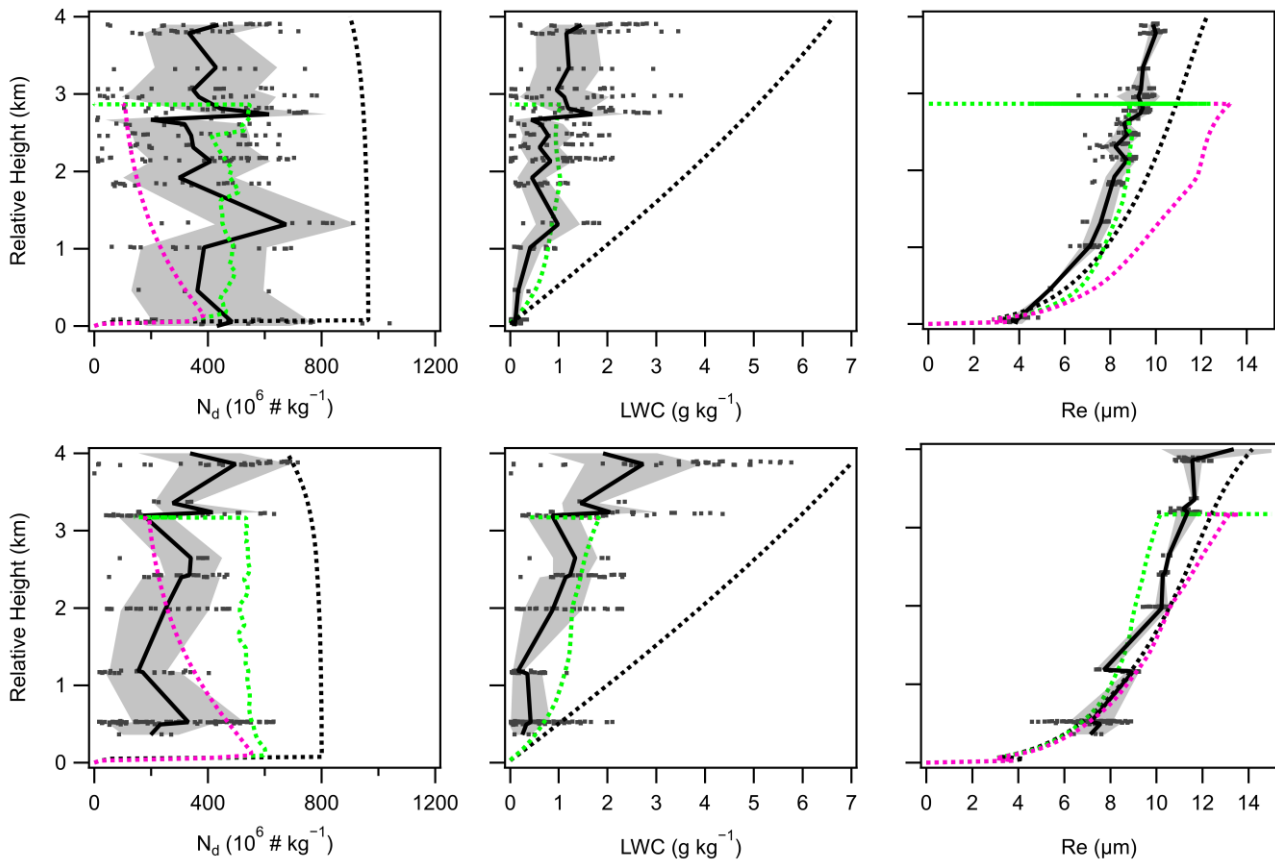
Figure 7: Vertical profiles of observed and simulated cloud droplet number concentration (N_d, kg^{-1}), LWC (g kg^{-1}) and effective
575   **radius (R_e, µm) for the Period 1-C300 case (upper plots) and the Period 2-C303 case (bottom plots). It is noted that, for consistency with the model, the units of N_d and LWC are expressed in "kg^{-1}", as opposed to "m^{-3}" in Sect. 3.3.1. The dots represent 1-hz measurements from the CDP. The solid black lines and shades represent average and standard deviation of observed values. The dashed black, pink and green lines represent simulations assuming adiabatic conditions, a mixture of inhomogeneous and homogeneous mixing, and the further inclusion of aerosol mixing respectively. The y-axis is the relative height with respect to the**
580   **LCL height. It is noted that the pink and green dashed lines overlap in the plots of LWC.**
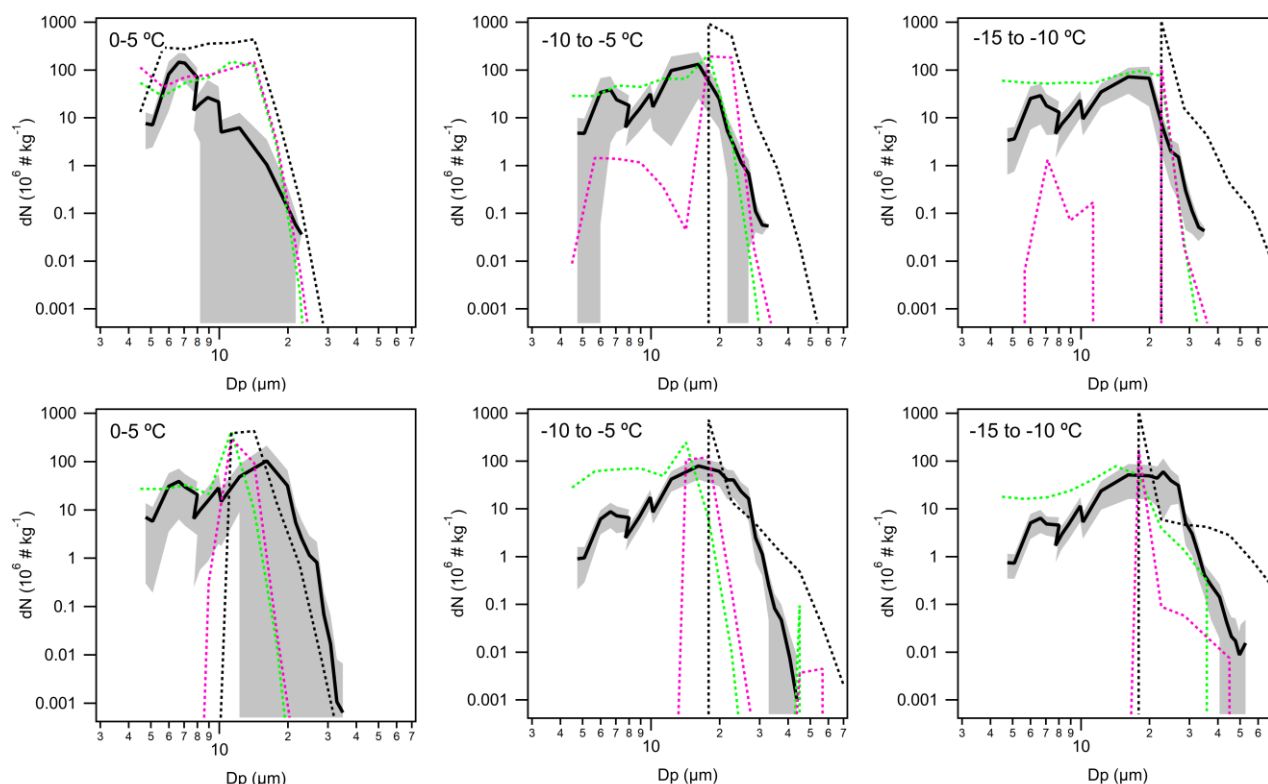
Figure 8: Observed and simulated cloud droplet size distributions for the Period 1-C300 case (upper plots) and the Period 2-C303 case (bottom plots), as a function of T ranging from near cloud base to high level. The solid black lines and shades represent average and standard deviation of observed values. The dashed black, pink and green lines represent simulations assuming adiabatic conditions, a mixture of inhomogeneous and homogeneous mixing, and the further inclusion of aerosol mixing respectively.

4 Conclusions and implications

In this study, observations during the DCMEX campaign (July to August 2022) provide a comprehensive characterization of thermodynamics, aerosol and cloud droplet properties in deep convective systems over the Magdalena Mountains, New Mexico. These novel datasets provide valuable insights into the influence of meteorological conditions and aerosol characteristics on the formation and growth of cloud droplets in this and similar regions during summer season in North America.

Backward dispersion analysis of the sampling region was conducted using the UK Met Office's NAME. NAME results indicate that the airmass sources were initially dominated by NW continental flow at the beginning of the campaign, later transitioning to predominantly SE oceanic flow. Observations revealed that the changes in airmass sources were associated with changes in meteorological parameters. The SE-flow dominated period was generally characterized by lower LCL heights, stronger convection, higher surface humidity and lower surface T compared to the NW-flow dominated period. An increase in the frequency and intensity of precipitation was observed from July 23. Aerosol observations further highlight the influence

22

of airmass sources and transport pathways on aerosol vertical distributions, size distributions, and chemical compositions, and subsequently their hygroscopic characteristics in this area. During the NW-flow period, N_a was observed from the surface up to altitudes above the LCL, while during the SE-flow period, N_a was mainly concentrated within the LCL layer, potentially due to more efficient in-cloud scavenging processes. An enhancement in small particles at high altitudes was mainly observed on days with relatively strong convection, indicating NPF processes at high altitudes in this deep-convective environment. Aerosol size distributions during the SE-flow period exhibited more pronounced bimodality compared to those observed during the NW-flow period. This was marked by an increase in Aitken-mode particle concentrations alongside generally fewer but larger accumulation-mode particles, suggesting greater cloud processing of aerosols under SE-flow conditions. The SE-flow period was also associated with larger sulfate mass fractions, more oxidized organic aerosol components, and subsequently greater hygroscopicity for submicron aerosols.

The observed changes in meteorological conditions and aerosol properties also influenced cloud droplet formation and growth, as indicated by CDP measurements. The SE-flow period generally presented higher ranges of LWC and R_e compared to the NW-flow period. The differences were attributed to higher cloud-base T and P (warmer and lower cloud bases), as well as changing aerosol characteristics (greater variability in aerosol concentration, size distributions, and hygroscopicity) during the SE-flow period. The enhanced range of R_e values (>12 µm) during the SE-flow period is likely correlated with the observed increase in precipitation, underling the critical role of both dynamic and microphysical factors in shaping cloud properties and precipitation processes under different flow regimes. Furthermore, a bin-microphysics parcel model was employed to simulate the formation and development of liquid cloud droplets under two representative conditions (NW-flow and SE-flow dominated periods) in this deep-convective system, which was constrained by meteorological and aerosol parameters derived from field measurements. Different scenarios were tested, including idealized adiabatic conditions and cases incorporating entrainment processes from the surrounding environment. The idealised adiabatic simulations produced cloud droplet size distributions that were too narrow and the vertical structure of N_d and LWC did not replicate observations. The model matched well with observations when considering entrainment processes from the surrounding environment, especially with the addition of aerosol mixing. The incorporation of aerosol mixing with entrainment processes is crucial in reproducing the width of droplet size distributions.

This study provides a valuable dataset for improving parameterizations of aerosol-cloud interactions and offers critical constraints for the accurate representation of microphysical processes in this area and similar deep convective systems for future model studies. The comparison between observations and bin-microphysics model simulations also highlights the importance of incorporating entrainment processes from surrounding environments, particularly aerosol mixing, in future simulations of deep convective clouds.

References

Aiken, A. C., Decarlo, P. F., Kroll, J. H., Worsnop, D. R., Huffman, J. A., Docherty, K. S., Ulbrich, I. M., Mohr, C., Kimmel, J. R., Sueper, D., Sun, Y., Zhang, Q., Trimborn, A., Northway, M., Ziemann, P. J., Canagaratna, M. R., Onasch, T. B., Alfarra, M. R., Prevot, A. S. H., Dommen, J., Duplissy, J., Metzger, A., Baltensperger, U., and Jimenez, J. L.: O/C and OM/OC ratios of primary, secondary, and ambient organic aerosols with highresolution time-of-flight aerosol mass spectrometry, Environ. Sci. Technol., 42, 4478–4485, https://doi.org/10.1021/es703009q, 2008.

Andreae, M. O., Afchine, A., Albrecht, R., Holanda, B. A., Artaxo, P., Barbosa, H. M. J., Borrmann, S., Cecchini, M. A., Costa, A., Dollner, M., Fütterer, D., Järvinen, E., Jurkat, T., Klimach, T., Konemann, T., Knote, C., Krämer, M., Krisna, T., Machado, L. A. T., Mertes, S., Minikin, A., Pöhlker, C., Pöhlker, M. L., Pöschl, U., Rosenfeld, D., Sauer, D., Schlager, H., Schnaiter, M., Schneider, J., Schulz, C., Spanu, A., Sperling, V. B., Voigt, C., Walser, A., Wang, J., Weinzierl, B., Wendisch, M., and Ziereis, H.: Aerosol characteristics and particle production in the upper troposphere over the Amazon Basin, Atmos. Chem. Phys., 18, 921–961, https://doi.org/10.5194/acp-18-921-2018, 2018.

Arakawa, A.: The cumulus parameterization problem: Past, present, and future, J. Climate, 17, 2493–2525, https://doi.org/10.1175/1520-0442(2004)017<2493:RATCPP>2.0.CO;2, 2004.

Baker, M. B., Corbin, R. G., and Latham, J.: The influence of entrainment on the evolution of cloud droplet spectra: I. A model of inhomogeneous mixing, Q. J. Roy. Meteor. Soc., 106, 581–598, https://doi.org/10.1002/qj.49710644914, 1980.

Blyth, A. M. and Latham, J.: Development of ice and precipitation in New Mexican summertime cumulus clouds, Q. J. Roy. Meteor. Soc., 119, 91–120, https://doi.org/10.1002/qj.49711950905, 1993.

Bott, A.: A flux method for the numerical solution of the stochastic collection equation, J. Atmos. Sci., 55, 2284–2293, 1998.

Braga, R. C., Rosenfeld, D., Weigel, R., Jurkat, T., Andreae, M. O., Wendisch, M., Pöschl, U., Voigt, C., Mahnke, C., Borrmann, S., Albrecht, R. I., Molleker, S., Vila, D. A., Machado, L. A. T., and Grulich, L.: Further evidence for CCN aerosol concentrations determining the height of warm rain and ice initiation in convective clouds over the Amazon basin, Atmos. Chem. Phys., 17, 14433–14456, https://doi.org/10.5194/acp-17-14433-2017, 2017a.

Braga, R. C., Rosenfeld, D., Weigel, R., Jurkat, T., Andreae, M. O., Wendisch, M., Pöhlker, M. L., Klimach, T., Pöschl, U., Pöhlker, C., Voigt, C., Mahnke, C., Borrmann, S., Albrecht, R. I., Molleker, S., Vila, D. A., Machado, L. A. T., and Artaxo, P.: Comparing parameterized versus measured microphysical properties of tropical convective cloud bases during the ACRIDICON–CHUVA campaign, Atmos. Chem. Phys., 17, 7365–7386, https://doi.org/10.5194/acp-17-7365-2017, 2017b.

Braga, R. C., Ervens, B., Rosenfeld, D., Andreae, M. O., Förster, J.-D., Fütterer, D., Hernández Pardo, L., Holanda, B. A., Jurkat-Witschas, T., Krüger, O. O., Lauer, O., Machado, L. A. T., Pöhlker, C., Sauer, D., Voigt, C., Walser, A., Wendisch, M., Pöschl, U., and Pöhlker, M. L.: Cloud droplet formation at the base of tropical convective clouds: closure between modeling and measurement results of ACRIDICON–CHUVA, Atmos. Chem. Phys., 21, 17513–17528, https://doi.org/10.5194/acp-21-17513-2021, 2021.

Braga, R. C., Rosenfeld, D., Andreae, M. O., Pöhlker, C., Pöschl, U., Voigt, C., Weinzierl, B., Wendisch, M., Pöhlker, M. L., and Harrison, D.: Detrainment dominates CCN concentrations around non-precipitating convective clouds over the Amazon, Geophys. Res. Lett., 49, e2022GL100411, https://doi.org/10.1029/2022GL100411, 2022.

680 Brown, A., Milton, S., Cullen, M., Golding, B., Mitchell, J., and Shelly, A.: Unified Modeling and Prediction of Weather and Climate: A 25-Year Journey, B. Am. Meteorol. Soc., 93, 1865–1877, https://doi.org/10.1175/bams-d-12-00018.1, 2012.

Burnet, F. and Brenguier, J.-L.: Observational Study of the Entrainment-Mixing Process in Warm Convective Clouds, J. Atmos. Sci., 64, 1995–2011, https://doi.org/10.1175/JAS3928.1, 2007.

Chandrakar, K. K., Cantrell, W., Chang, K., Ciochetto, D., Niedermeier, D., Ovchinnikov, M., Shaw, R. A., and Yang, F.:
685 Aerosol Indirect Effect from Turbulence-Induced Broadening of CloudDroplet Size Distributions, P. Natl. Acad. Sci. USA, 113, 14243– 14248, https://doi.org/10.1073/pnas.1612686113, 2016.

Chang, R. Y.-W., Slowik, J. G., Shantz, N. C., Vlasenko, A., Liggio, J., Sjostedt, S. J., Leaitch, W. R., and Abbatt, J. P. D.: The hygroscopicity parameter (κ) of ambient organic aerosol at a field site subject to biogenic and anthropogenic influences: relationship to degree of aerosol oxidation, Atmos. Chem. Phys., 10, 5047–5064, https://doi.org/10.5194/acp-10-5047-2010,
690 2010.

Drewnick, F., Hings, S. S., DeCarlo, P., Jayne, J. T., Gonin, M., Fuhrer, K., Weimer, S., Jimenez, J. L., Demerjian, K. L., Borrmann, S., and Worsnop, D. R.: A new time-of-flight aerosol mass spectrometer (TOF-AMS) – Instrument description and first field deployment, Aerosol Sci. Tech., 39, 637–658, https://doi.org/10.1080/02786820500182040, 2005.

Dusek, U., Frank, G. P., Hildebrandt, L., Curtius, J., Schneider, J., Walter, S., Chand, D., Drewnick, F., Hings, S., Jung, D.,
695 Borrmann, S., and Andreae, M. O.: Size matters more than chemistry for cloud-nucleating ability of aerosol particles, Science, 312, 1375–1378, https://doi.org/10.1126/science.1125261, 2006.

Ekman Annica, M. L., Wang, C., Ström, J., and Krejci, R.: Explicit Simulation of aerosol physics in a cloud-resolving model: aerosol transport and processing in the free troposphere, J. Atmos. Sci., 63, 682–696, https://doi.org/10.1175/JAS3645.1, 2006.

Fan, J., Leung, L. R., Rosenfeld, D., Chen, Q., Li, Z., Zhang, J., and Yan, H.: Microphysical Effects Determine Macrophysical
700 Response for Aerosol Impacts on Deep Convective Clouds, P. Natl. Acad. Sci. USA, 110, E4581–E4590, https://doi.org/10.1073/pnas.1316830110, 2013.

Fan, J., Rosenfeld, D., Zhang, Y., Giangrande, S. E., Li, Z., Machado, L. A. T., Martin, S. T., Yang, Y., Wang, J., Artaxo, P., Barbosa, H. M. J., Braga, R. C., Comstock, J. M., Feng, Z., Gao, W., Gomes, H. B., Mei, F., Pöhlker, C., Pöhlker, M. L., Pöschl, U., and Souza, R. A. F.: Substantial convection and precipitation enhancements by ultrafine aerosol particles, Science,
705 359, 411– 418, https://doi.org/10.1126/science.aan8461, 2018.

Farmer, D. K., Cappa, C. D., and Kreidenweis, S. M.: Atmospheric Processes and Their Controlling Influence on Cloud Condensation Nuclei Activity, Chem. Rev., 115, 4199–4217, https://doi.org/10.1021/cr5006292, 2015.

Finney, D. L., Blyth, A. M., Gallagher, M., Wu, H., Nott, G. J., Biggerstaff, M. I., Sonnenfeld, R. G., Daily, M., Walker, D., Dufton, D., Bower, K., Böing, S., Choularton, T., Crosier, J., Groves, J., Field, P. R., Coe, H., Murray, B. J., Lloyd, G., Marsden,
710 N. A., Flynn, M., Hu, K., Thamban, N. M., Williams, P. I., Connolly, P. J., McQuaid, J. B., Robinson, J., Cui, Z., Burton, R.

R., Carrie, G., Moore, R., Abel, S. J., Tiddeman, D., and Aulich, G.: Deep Convective Microphysics Experiment (DCMEX) coordinated aircraft and ground observations: microphysics, aerosol, and dynamics during cumulonimbus development, Earth Syst. Sci. Data, 16, 2141–2163, https://doi.org/10.5194/essd-16-2141-2024, 2024.

Fowler, K., Connolly, P., and Topping, D.: Modelling the effect of condensed-phase diffusion on the homogeneous nucleation of ice in ultra-viscous particles, Atmos. Chem. Phys., 20, 683–698, https://doi.org/10.5194/acp-20-683-2020, 2020.

Han, S., Hong, J., Luo, Q., Xu, H., Tan, H., Wang, Q., Tao, J., Zhou, Y., Peng, L., He, Y., Shi, J., Ma, N., Cheng, Y., and Su, H.: Hygroscopicity of organic compounds as a function of organic functionality, water solubility, molecular weight, and oxidation level, Atmos. Chem. Phys., 22, 3985–4004, https://doi.org/10.5194/acp-22-3985-2022, 2022.

Haslett, S. L., Taylor, J. W., Deetz, K., Vogel, B., Babić, K., Kalthoff, N., Wieser, A., Dione, C., Lohou, F., Brito, J., Dupuy, R., Schwarzenboeck, A., Zieger, P., and Coe, H.: The radiative impact of out-of-cloud aerosol hygroscopic growth during the summer monsoon in southern West Africa, Atmos. Chem. Phys., 19, 1505–1520, https://doi.org/10.5194/acp-19-1505-2019, 2019.

Hering, S. V., Stolzenburg, M. R., Quant, F. R., Oberreit, D. R., and Keady, P. B.: A Laminar-Flow, Water-Based Condensation Particle Counter (WCPC), Aerosol Sci. Tech., 39, 659–672, https://doi.org/10.1080/02786820500182123, 2005.

Hoffmann, E. H., Tilgner, A., Schrödner, R., Bräuer, P., Wolke, R., and Herrmann, H.: An advanced modeling study on the impacts and atmospheric implications of multiphase dimethyl sulfide chemistry, P. Natl. Acad. Sci. USA, 113, 11776–11781, https://doi.org/10.1073/pnas.1606320113, 2016.

Hoppel, W. A., Fitzgerald, J. W., and Larson, R. E.: Aerosol size distributions in air masses advecting off the east coast of the United States, J. Geophys. Res.-Atmos., 90, 2365–2379, https://doi.org/10.1029/JD090iD01p02365, 1985.

Houze Jr., R. A.: Cloud Dynamics, Academic press, Oxford UK, ISBN 978-0-12-374266-7, 1–432, 2014.

Jacobson, M. Z.: Fundamentals of Atmospheric Modeling, in: 2nd Ed., Cambridge University Press, https://doi.org/10.1017/CBO9781139165389, 2005.

James, R. L., Crosier, J., and Connolly, P. J.: A bin microphysics parcel model investigation of secondary ice formation in an idealised shallow convective cloud, Atmos. Chem. Phys., 23, 9099–9121, https://doi.org/10.5194/acp-23-9099-2023, 2023.

Jensen, M. P. and Del Genio, A. D.: Radiative and microphysical characteristics of deep convective systems in the tropical western Pacific, J. Appl. Meteorol., 42, 1234–1254, https://doi.org/10.1175/1520-0450(2003)042<1234:RAMCOD>2.0.CO;2, 2003.

Jiang, J. H., Su, H., Huang, L., Wang, Y., Massie, S., Zhao, B., Omar, A., and Wang, Z.: Contrasting effects on deep convective clouds by different types of aerosols, Nat. Commun., 9, 3874, https://doi.org/10.1038/s41467-018-06280-4, 2018.

Jones, A., Thomson, D., Hort, M., and Devenish, B.: The UK Met Office's next-generation atmospheric dispersion model, NAME III, Air Pollut. Model. Appl. XVII, 17, 580–589, https://doi.org/10.1007/978-0-387-68854-1_62, 2007.

Koren, I., Martins, J. V., Remer, L. A., and Afargan, H.: Smoke invigoration versus inhibition of clouds over the Amazon, Science, 321, 946–949, https://doi.org/10.1126/science.1159185, 2008.

Koren, I., Feingold, G., and Remer, L. A.: The invigoration of deep convective clouds over the Atlantic: aerosol effect,
745   meteorology or retrieval artifact?, Atmos. Chem. Phys., 10, 8855–8872, https://doi.org/10.5194/acp-10-8855-2010, 2010.

Koren, I., Dagan, G., and Altaratz, O.: From aerosol-limited to invigoration of warm convective clouds, Science, 344, 1143–
1146, https://doi.org/10.1126/science.1252595, 2014.

Korolev, A. V. , McFarquhar, G., Field, P. R., Franklin, C., Lawson, P., Wang, Z., Williams, E., Abel, S. J., Axisa, D.,
Borrmann, S., Crosier, J., Fugal, J., Krämer, M., Lohmann, U., Schlenczek, O., Schnaiter, M., and Wendisch, M.: MixedPhase
750   Clouds: Progress and Challenges, Meteor. Mon., 58, 5.1–5.50, https://doi.org/10.1175/AMSMONOGRAPHS-D-170001.1,
2017.

Kulmala, M., Kontkanen, J., Junninen, H., Lehtipalo, K., Manninen, H., Nieminen, T., Petaja, T., Sipila, M., Schobesberger,
S., Rantala, P., Franchin, A., Jokinen, T., Jarvinen, E., Aijala, M., Kangasluoma, J., Hakala, J., Aalto, P., Paasonen, P., Mikkila,
J., Vanhanen, J., Aalto, J., Hakola, H., Makkonen, U., Ruuskanen, T., Mauldin, R., Duplissy, J., Vehkamaki, H., Back, J.,
755   Kortelainen, A., Riipinen, I., Kurten, T., Johnston, M., Smith, J., Ehn, M., Mentel, T., Lehtinen, K., Laaksonen, A., Kerminen,
V., and Worsnop, D.: Direct Observations of Atmospheric Aerosol Nucleation, Science, 339, 943-946,
https://doi:10.1126/science.1227385, 2013.

Lance, S., Brock, C. A., Rogers, D., and Gordon, J. A.: Water droplet calibration of the Cloud Droplet Probe (CDP) and in-
flight performance in liquid, ice and mixed-phase clouds during ARCPAC, Atmos. Meas. Tech., 3, 1683–1706,
760   https://doi.org/10.5194/amt-3-1683-2010, 2010.

Lehmann, K., Siebert, H., and Shaw, R. A.: Homogeneous and Inhomogeneous Mixing in Cumulus Clouds: Dependence on
Local Turbulence Structure, J. Atmos. Sci., 66, 3641–3659, https://doi.org/10.1175/2009JAS3012.1, 2009.

Li, Z., Niu, F., Fan, J., Liu, Y., Rosenfeld, D., and Ding, Y.: Long-term impacts of aerosols on the vertical development of
clouds and precipitation, Nat. Geosci., 4, 888–894, https://doi.org/10.1038/ngeo1313, 2011.

765   Liu, D., Flynn, M., Gysel, M., Targino, A., Crawford, I., Bower, K., Choularton, T., Jurányi, Z., Steinbacher, M., Hüglin, C.,
Curtius, J., Kampus, M., Petzold, A., Weingartner, E., Baltensperger, U., and Coe, H.: Single particle characterization of black
carbon aerosols at a tropospheric alpine site in Switzerland, Atmos. Chem. Phys., 10, 7389–7407,
https://doi.org/10.5194/acp10-7389-2010, 2010.

Long, A. B.: Solutions to the Droplet Collection Equation for Polynomial Kernels, J. Atmos. Sci., 31, 1040–1052,
770   https://doi.org/10.1175/1520- 0469(1974)0312.0.CO;2, 1974.

May, R. M., Goebbert, K. H., Thielen, J. E., Leeman, J. R., Camron, M. D., Bruick, Z., Bruning, E. C., Manser, R. P., Arms,
S. C., and Marsh, P. T.: MetPy: A Meteorological Python Library for Data Analysis and Visualization, B. Am. Meteorol. Soc.,
103, E2273– E2284, https://doi.org/10.1175/BAMS-D-21-0125.1, 2022.

Middlebrook, A. M., Bahreini, R., Jimenez, J. L., and Canagaratna, M. R.: Evaluation of composition-dependent collection
775   efficiencies for the aerodyne aerosol mass spectrometer using field data, Aerosol Sci. Tech., 46, 258–271,
https://doi.org/10.1080/02786826.2011.620041, 2012.

Morgan, W. T., Allan, J. D., Bower, K. N., Highwood, E. J., Liu, D., McMeeking, G. R., Northway, M. J., Williams, P. I., Krejci, R., and Coe, H.: Airborne measurements of the spatial distribution of aerosol chemical composition across Europe and evolution of the organic fraction, Atmos. Chem. Phys., 10, 4065–4083, https://doi.org/10.5194/acp-10-4065-2010, 2010.

780 Morgan, W. T., Allan, J. D., Bauguitte, S., Darbyshire, E., Flynn, M. J., Lee, J., Liu, D., Johnson, B., Haywood, J., Longo, K. M., Artaxo, P. E., and Coe, H.: Transformation and ageing of biomass burning carbonaceous aerosol over tropical South America from aircraft in situ measurements during SAMBBA, Atmos. Chem. Phys., 20, 5309–5326, https://doi.org/10.5194/acp-20-5309-2020, 2020.

Newman, R., and Noy, I.: The global costs of extreme weather that are attributable to climate change, Nat. Commun., 14, 6103,
785 https://doi.org/10.1038/s41467-023-41888-1, 2023.

Petters, M. D. and Kreidenweis, S. M.: A single parameter representation of hygroscopic growth and cloud condensation nucleus activity, Atmos. Chem. Phys., 7, 1961–1971, https://doi.org/10.5194/acp-7-1961-2007, 2007.

Pimlott, M. A., Pope, R. J., Kerridge, B. J., Latter, B. G., Knappett, D. S., Heard, D. E., Ventress, L. J., Siddans, R., Feng, W., and Chipperfield, M. P.: Investigating the global OH radical distribution using steady-state approximations and satellite data,
790 Atmos. Chem. Phys., 22, 10467–10488, https://doi.org/10.5194/acp-22-10467-2022, 2022.

Pöhlker, M. L., Pöhlker, C., Quaas, J., Mülmenstädt, J., Pozzer, A., Andreae, M. O., Artaxo, P., Block, K., Coe, H., Ervens, B., Gallimore, P., Gaston, C. J., Gunthe, S. S., Henning, S., Herrmann, H., Krüger, O. O., McFiggans, G., Poulain, L., Raj, S. S., Reyes-Villegas, E., Royer, H. M., Walter, D., Wang, Y., and Pöschl, U.: Global organic and inorganic aerosol hygroscopicity and its effect on radiative forcing, Nat. Commun., 14, 6139, https://doi.org/10.1038/s41467-023-41695-8, 2023.

795 Pruppacher, H. R. and Klett, J. D.: Microphysics of Clouds and Precipitation, in: 2nd Edn., Springer, Dordrecht, https://doi.org/10.1007/978-0-306-48100-0, 2010.

Ramanathan, V., Ramana, M. V., Roberts, G., Kim, D., Corrigan, C., Chung, C., and Winker, D.: Warming trends in Asia amplified by brown cloud solar absorption, Nature, 448, 575–578, https://doi.org/10.1038/nature06019, 2007.

Rosenberg, P. D., Dean, A. R., Williams, P. I., Dorsey, J. R., Minikin, A., Pickering, M. A., and Petzold, A.: Particle sizing
800 calibration with refractive index correction for light scattering optical particle counters and impacts upon PCASP and CDP data collected during the Fennec campaign, Atmos. Meas. Tech., 5, 1147–1163, https://doi.org/10.5194/amt-5-1147-2012, 2012.

Rosenfeld, D., Lohmann, U., Raga, G. B., O'Dowd, C. D., Kulmala, M., Fuzzi, S., Reissell, A., and Andreae, M. O.: Flood or drought: How do aerosols affect precipitation?, Science, 321, 1309–1313, https://doi.org/10.1126/science.1160606, 2008.

805 Rosenfeld, D., Yu, X., Liu, G., Xu, X., Zhu, Y., Yue, Z., Dai, J., Dong, Z., Dong, Y., and Peng, Y.: Glaciation temperatures of convective clouds ingesting desert dust, air pollution and smoke from forest fires, Geophys. Res. Lett., 38, 2006–2010, https://doi.org/10.1029/2011GL049423, 2011.

Rosenfeld, D., Wang, H., and Rasch, P. J.: The roles of cloud drop effective radius and LWP in determining rain properties in marine stratocumulus, Geophys. Res. Lett., 39, 1–6, https://doi.org/10.1029/2012GL052028, 2012.

810 Rosenfeld, D., Sherwood, S., Wood, R., and Donner, L.: Atmospheric science. Climate effects of aerosol-cloud interactions, Science, 343, 379–380, https://doi.org/10.1126/science.1247490, 2014.

Stull, R.: Practical meteorology: an algebra-based survey of atmospheric science, University of British Columbia, ISBN-10: 0888651767, ISBN-13: 978-0888651761, 2016.

Tao, W., Chen, J., Li, Z., Wang, C., and Zhang, C.: Impact of aerosols on convective clouds and precipitation, Rev. Geophys.,
815 50, RG2001, https://doi.org/10.1029/2011RG000369, 2012.

Tashmim, L., Porter, W. C., Chen, Q., Alexander, B., Fite, C. H., Holmes, C. D., Pierce, J. R., Croft, B., and Ishino, S.: Contribution of expanded marine sulfur chemistry to the seasonal variability of dimethyl sulfide oxidation products and size-resolved sulfate aerosol, Atmos. Chem. Phys., 24, 3379–3403, https://doi.org/10.5194/acp-24-3379-2024, 2024.

Varble, A. C., Igel, A. L., Morrison, H., Grabowski, W. W., and Lebo, Z. J.: Opinion: A critical evaluation of the evidence for
820 aerosol invigoration of deep convection, Atmos. Chem. Phys., 23, 13791–13808, https://doi.org/10.5194/acp-23-13791-2023, 2023.

Villanueva-Fierro, I., Popp, C. J., and Martin, R. S.: Biogenic emissions and ambient concentrations of hydrocarbons, carbonyl compounds and organic acids from ponderosa pine and cottonwood trees at rural and forested sites in Central New Mexico, Atmos. Environ., 38, 249–260, https://doi.org/10.1016/j.atmosenv.2003.09.051, 2004.

825 Wang, Y., Wang, M., Zhang, R., Ghan, S. J., Lin, Y., Hu, J., Pan, B., Levy, M., Jiang, J. H., and Molina, M. J.: Assessing the effects of anthropogenic aerosols on Pacific storm track using a multiscale global climate model, P. Natl. Acad. Sci. USA, 111, 6894–6899, https://doi.org/10.1073/pnas.1403364111, 2014.

Williamson, C. J., Kupc, A., Axisa, D., Bilsback, K. R., Bui, T., Campuzano-Jost, P., Dollner, M., Froyd, K. D., Hodshire, A. L., Jimenez, J. L., Kodros, J. K., Luo, G., Murphy, D. M., Nault, B. A., Ray, E. A., Weinzierl, B., Wilson, J. C., Yu, F., Yu,
830 P., Pierce, J. R., and Brock, C. A.: A large source of cloud condensation nuclei from new particle formation in the tropics, Nature, 574, 399–403, https://doi.org/10.1038/s41586-019-1638-9, 2019.

Wu, H., Taylor, J. W., Szpek, K., Langridge, J. M., Williams, P. I., Flynn, M., Allan, J. D., Abel, S. J., Pitt, J., Cotterell, M. I., Fox, C., Davies, N. W., Haywood, J., and Coe, H.: Vertical variability of the properties of highly aged biomass burning aerosol transported over the southeast Atlantic during CLARIFY-2017, Atmos. Chem. Phys., 20, 12697–12719,
835 https://doi.org/10.5194/acp-20-12697-2020, 2020.

Yin, J., Pan, Z., Mao, F., Rosenfeld, D., Zhang, L., Chen, J., and Gong, J.: Large effects of fine and coarse aerosols on tropical deep convective systems throughout their lifecycle, npj Clim Atmos Sci, 7, 195, https://doi.org/10.1038/s41612-024-00739-6, 2024.

Yum, S. S. and Hudson, J. G.: Adiabatic predictions and observations of cloud droplet spectral broadness, Atmos. Res., 73,
840 203– 223, https://doi.org/10.1016/j.atmosres.2004.10.006, 2005.

Zhao, B., Shrivastava, M., Donahue, N. M., Gordon, H., Schervish, M., Shilling, J. E., Zaveri, R. A., Wang, J., Andreae, M. O., Zhao, C., Gaudet, B., Liu, Y., Fan, J. W., and Fast, J. D.: High concentration of ultrafine particles in the Amazon free

troposphere produced by organic new particle formation, P. Natl. Acad. Sci., 117, 25344–25351, https://doi.org/10.1073/pnas.2006716117, 2020.

845 Zhao, Y., Saunois, M., Bousquet, P., Lin, X., Berchet, A., Hegglin, M. I., Canadell, J. G., Jackson, R. B., Hauglustaine, D. A., Szopa, S., Stavert, A. R., Abraham, N. L., Archibald, A. T., Bekki, S., Deushi, M., Jöckel, P., Josse, B., Kinnison, D., Kirner, O., Marécal, V., O'Connor, F. M., Plummer, D. A., Revell, L. E., Rozanov, E., Stenke, A., Strode, S., Tilmes, S., Dlugokencky, E. J., and Zheng, B.: Inter-model comparison of global hydroxyl radical (OH) distributions and their impact on atmospheric methane over the 2000–2016 period, Atmos. Chem. Phys., 19, 13701–13723, https://doi.org/10.5194/acp-19-13701-2019,
850 2019.

Zhou, J.: Hygroscopic Properties of Atmospheric Aerosol Particles in Various Environments, Doctoral dissertation, Lund University, Lund, Sweden, ISBN 91-7874-120-3, 14–20, 2001.